UNIVERSITÀ DEGLI STUDI DI MILANO

FACOLTÀ DI SCIENZE E TECNOLOGIE

Laurea in Scienze Chimiche

Reaction rate constants in condensed phase

A numerically exact quantum study

Relatore:
Prof. Rocco MARTINAZZO

Tesi di Dottorato di:
Ambra SIBILLA

Anno accademico 2019-2020

"El destino suele estar a la vuelta de la esquina.
Como si fuese un chorizo, una furcia o un vendedor de lotería:
sus tres encarnaciones más socorridas.
Pero lo que no hace es visitas a domicilio.
Hay que ir a por él."

Carlos Ruíz Zafón

Contents

Chapter 1

Introduction

In order to study a condensed phase reaction it is necessary to understand the effects of the environment on the chemical process, extremely challenging when light atoms and low temperatures are involved, because of the resultant not negligible quantum effects. The focus of this thesis is the calculation of kinetic constants for this kind of system, applying a fully-quantum investigation in order to correctly describe the dynamics in such extreme conditions.

Figure 1.1: The Orion Nebula in infrared from HAWK-I [1].

1.1 Thesis overview

The long term aim of this project was the interaction between Hydrogen atoms and graphene-like surfaces, typical condensed-phase processes. In particular we were interested in the *InterStellar Medium* (ISM) environment, where the extremely low temperature, combined with the relevant wave-like behavior of a light atom such as H, makes quantum effects not negligible.

The main theoretical challenge lies in the huge computational cost required by an exact quantum calculation. Indeed, in order to model a surface, we need to consider a high number of degrees of freedom, which leads to an exponential increase of the computational time. However, since the substrate importance essentially resides in its capability to activate the process and its role in reaching an equilibrium, we can approximate the environment as an ensemble of independent Harmonic Oscillators (HOs), called *bath*, coupled with the main *system* (H atom). With this strategy we can simulate the reaction dynamics taking into account the quantum coherence, the thermal fluctuations and the dissipation of energy excess generated during the reaction, and strongly reduce the computational cost. In order to perform the dynamics of the entire setup (system+bath) we exploited a high-dimensional wave-packet technique, the *MultiConfiguration Time-Dependent Hartree* (MCTDH) approach, computationally cheaper than standard quantum dynamics methods, operating with the *Multi Layer* (ML) extension of the Heidelberg package. Combining a Monte Carlo sampling of the initial bath state (described with both normal and effective mode representation) with the means of MCTDH dynamics, we obtained thermal rate constants for several temperatures and system-bath friction values.

In order to model the condensed-phase processes we were interested in, we considered at first a simple problem described by a symmetric monodimensional potential, useful as diffusion model. We tested the methodology comparing our results with the ones obtained with other techniques, investigating a wide range of reaction regimes and focusing on the quantum-classical crossover. Our results obtained at very low temperatures have been used as benchmarks for the *Ring Polymer Instanton* (RPI) technique, employed in the Theoretical Molecular Quantum Dynamics research group of Professor Jeremy Richardson, at the Swiss Federal Institute of Technology in Zurich (ETH).

Once a full study of the symmetric problem was conducted, we switched to an asymmetrical potential (again monodimensional) that can be a first approximation of a phenomenon involved in the hydrogen formation in interstellar clouds (Fig. 1.1): the transition from the physisorption well to the chemisorption one of H atoms on interstellar dust grains.

1.2 Examples of reactions in condensed phase

Condensed phase reactions include a wide range of processes that can occur in solution or on solid substrates. In this section we show the ones of major interest nowadays: proteins proton-transfer mechanisms in biological environment and processes occurring at gas-solid interfaces.

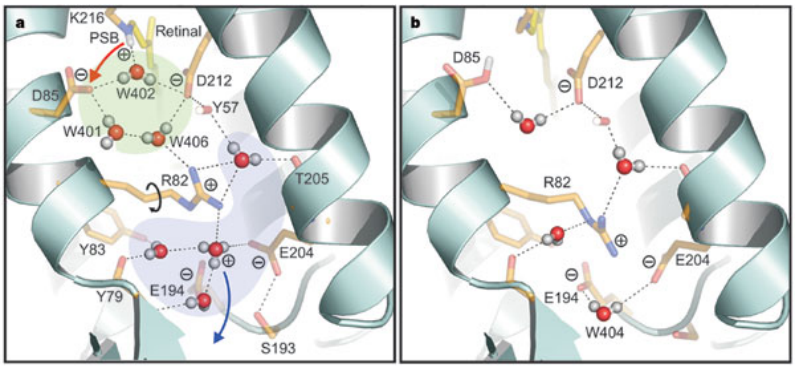

Figure 1.2: Hydrogen transfer in protein [2].

1.2.1 Proton transfer in protein

Natural processes, such as respiration, vision, photosynthesis and DNA mutation, require highly efficient charge and energy transport through biomolecules (Fig. 1.2), for which quantum effects turned out to be crucial.

Several experimental and theoretical studies proved that charge transfer takes place due to proton hopping from one site to another through tunneling [3]. For this reason the dynamics of this phenomenon depends on hydrogen coupling with the protein environment, that facilitates the transfer from a donor to an acceptor through its thermal fluctuations.

The hopping model implies that charge propagates in multiple steps along the proteins from one localized state to another, but experiments on hole transfer in DNA revealed transfer rates which are not dependent on the path (bridge) length [4]. This has been explained considering the quantum phenomenon of delocalization, supported by the rigid molecular structure of DNA. Indeed, the charge transfer mechanism of this biological system is not the simple hopping due to tunneling, but it consists instead in a single step transition from a localized hole state to delocalized states, spread over the entire bridge [4].

1.2.2 Hydrogen sticking and diffusion on graphene

Interactions between hydrogen atoms and a graphene sheet or other carbon materials are topics of ever growing interest in the scientific community. This is due to the possibility of easily modulating the electric, optical and magnetic properties of graphene-like structures (Fig. 1.3). Their interactions with hydrogen atoms play a leading role in several fields such as astrophysics, nuclear fusion, hydrogen storage and carbon-based technology [5].

The two main processes of interest when hydrogen and graphene (or similar-behaving carbon structures) interact are diffusion and sticking. Wave-packet calculations estimate the site-to-site hopping at temperature $T = 0$ K and found that physisorbed H atoms do not stay at rest in their equilibrium position even in these conditions, i.e. in absence of thermal fluctuations [8]. When the hydrogen atom is in a physisorbed state, its coupling with the substrate is very weak, and this allows for considerable simplifications when simulating its quantum dynamics. Sticking probability including surface corrugation have been found to be less than the 0.05%

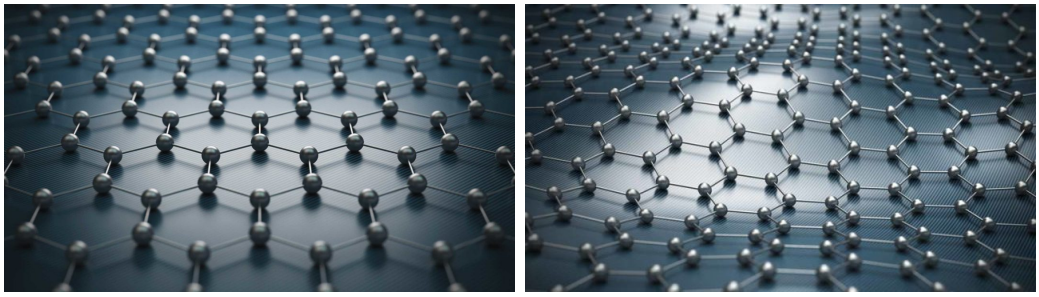

Figure 1.3: Representation of a carbon surface, planar on the left [6] and corrugated on the right [7].

for energies in the range 0-25 meV [9]. As the dynamic corrugation of the surface is increased by the temperature [5], the sticking increases as well, but this also drastically raises the desorption probability from the surface. Unfortunately, experiments at really low temperature in which H atoms can physisorb while remaining stable on the surface [10][11][12] are really difficult to conduct. For this reason, no experimental results are available for the H atom sticking coefficient at energies of a few meV. In contrast, when a chemical bond between the H atom and the surface is formed (chemisorption regime), the presence of an adsorption barrier and the stronger coupling play a primary role in determining the sticking probability.

1.2.3 H_2 formation in the interstellar medium

H_2 is the most abundant molecular species in the entire Universe, plays a key role in the formation of complex chemicals and acts as a radiative cooler during the gravitational collapse of interstellar clouds, the first step in the formation of star and complex galactic structures.

In the InterStellar Medium (ISM) the accumulation of molecular hydrogen is extremely difficult, because of the presence of intense UV radiations that easily dissociate it. Moreover, when molecular formation occurs in vacuum, the excess

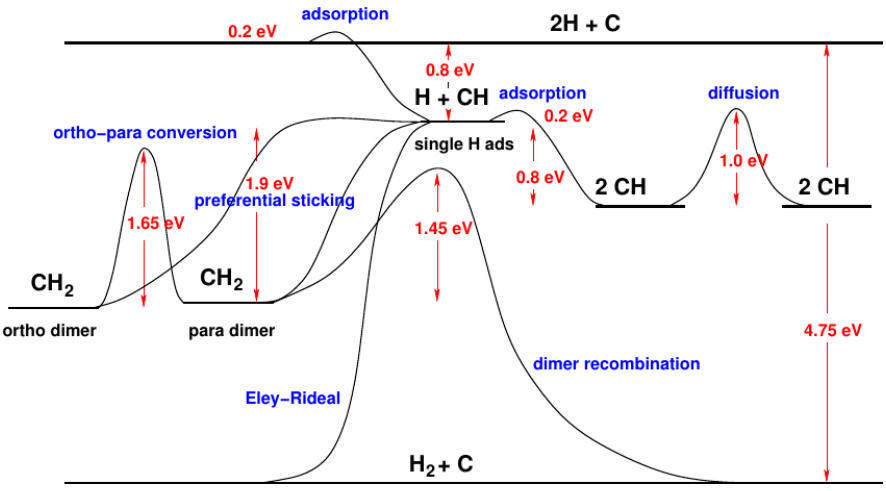

Figure 1.4: Schematic view of possible reaction steps in the formation of molecular hydrogen at the gas-graphene interface [14].

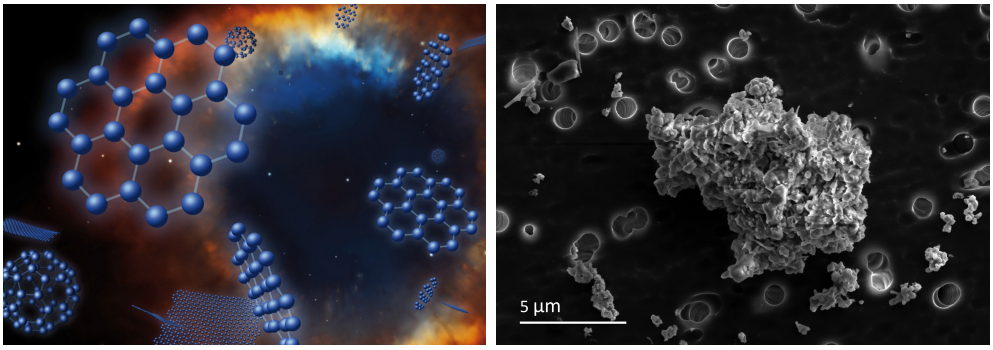

Figure 1.5: Left: PAHs in the interstellar medium [15]; right: interstellar dust grain [16].

energy of reaction (the binding *plus* the collision energy) is hardly dissipated before the reaction complex breaks up [13]. Despite this, H_2 is the most abundant molecule in the ISM, thus its formation mechanism has to be extremely efficient.

There are several possible reaction pathways that promote the formation of molecular hydrogen in the ISM, schematically represented in Fig. 1.4, and they are catalyzed by a carbonaceous substrate, that can be a Polyclinic Aromatic Hydrocarbon (PAH) or an interstellar dust grain (Fig. 1.6), the "soot" condensing from the outflows of stars in the asymptotic giant branch. The two main mechanisms are the *Eley-Rideal* and the *Langmuir–Hinshelwood*. In the first case a H atom in gas phase collides with another H atom chemically bound to a C atom of the substrate:

$$H_{(g)} + C_{(s)} \rightarrow CH_{(chem)}$$

$$H_{(g)} + CH_{(chem)} \rightarrow H_2 + C_{(s)}$$

while in the second one two H atoms physisorbed on the surface (free to diffuse) interact:

$$H_{(g)} + C_{(s)} \rightarrow CH_{(phys)}$$

$$2CH_{(phys)} \rightarrow H_2 + C_{(s)}$$

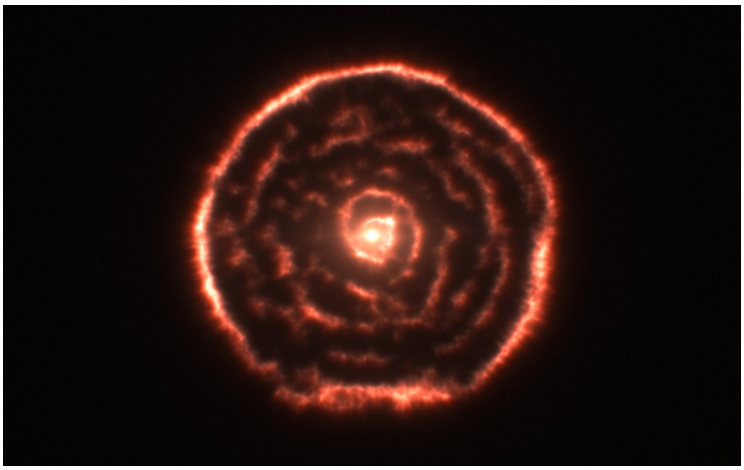

Figure 1.6: Spiral structure of material around the old star R Sculptoris, an example of Asymptotic Giant Brunch (AGB) star [17].

Thus, the first step for each of the above reactions is always the adsorption, either physical or chemical, of H atoms on the carbon surface which then dissipates the excess energy released from the H-H bond formation.

1.3 Quantum vs classical regime

In order to investigate dynamical phenomena at different temperature and friction regimes, one needs to describe the role of the environment thanks to which a kinetic regime can be established. Its presence is fundamental to dissipate the excess energy released by the reaction, and provides the necessary mechanism for its activation: thermal fluctuations at high temperatures and quantum fluctuations (tunneling out of a metastable state) at low temperatures. A crossover temperature T_c between these two regimes exists for every process [18][19], and it is given by

$$T_c = \frac{\hbar \lambda_0}{2\pi k_B} \tag{1.1}$$

where $\hbar$ is the reduced Plank constant, λ_0 is the effective imaginary frequency at the top of the activation barrier, and k_B is the Boltzmann constant [20][21]. The physical meaning of the crossover will be explained in Chapter 5.

1.3.1 Isomerization potential

For the generic isomerization potential path shown in Fig. 1.7, the only possible event is the transition from one well to the other, and this reaction may occur through two different mechanisms: classically, thermal activation is needed to overcome the potential barrier, while in quantum regime this is not required.

At high temperature the environment provides energy to the particle in the reagent well and activates the reaction by fluctuations, the reactant overcomes the barrier and reaches the equilibrium in the product well when the excess energy is dissipated into the environment. Both of these phenomena, i.e. fluctuation and energy dissipation, increase with friction, with opposite effects on the reaction kinetics. This affects the trend of the kinetic constant as a function of friction, characterized by the particular *turnover* behaviour predicted by Kramers in the middle of the last century [22]. For extremely low friction fluctuations rule the dynamics, because the

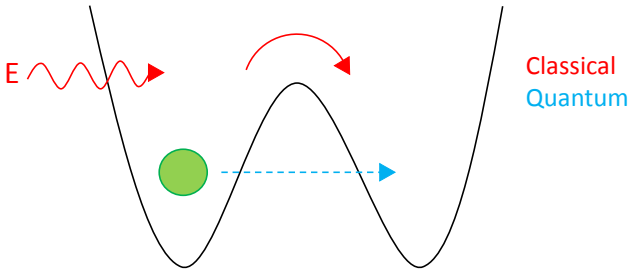

Figure 1.7: Schematic representation of classical and quantum mechanisms for the isomerization process.

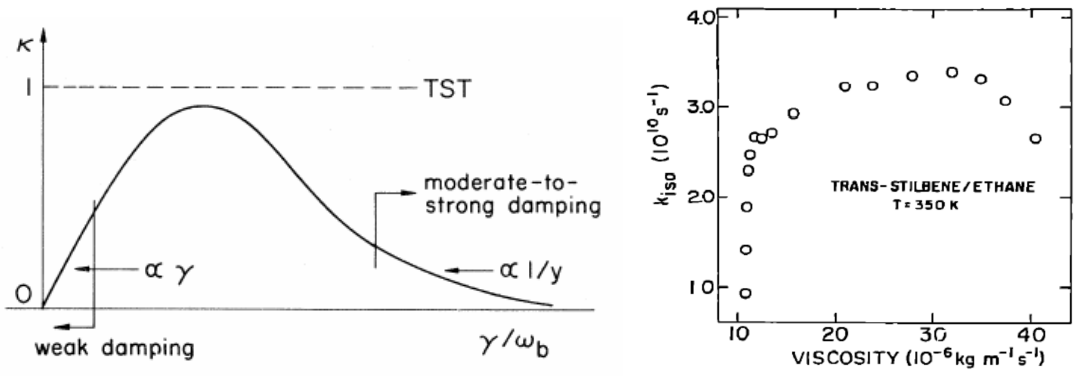

Figure 1.8: Theoretical representation [23] (left) and experimental proof [24] (right) of Kramers' turnover.

system-bath interaction is too weak for damping, hence the kinetic constant proportionally increases with the friction coefficient. At strong friction on the other hand, fluctuations become of secondary importance and the reaction slows down because the motion in configuration space is damped, thus we observe a decrease in the rate constant. This theoretical trend was experimentally observed by Minyung et al. [24], who studied the kinetics of the isomerization reaction from trans-stilbene to ethane, varying the solvent viscosity (i.e. what we called friction) while keeping fixed the temperature (Fig. 1.8).

At low temperature thermal activation is negligible. The reaction occurs because the system tunnels out of the metastable well in which it is initially trapped. Here, the key observation is that the tunneling rate decreases exponentially with the friction coefficient, at least for small values. Since at large values the effect of friction is, as above, to damp the motion in coordinate space, the kinetic constant shows an overall monotonic decrease as a function of friction [25].

1.3.2 Physisorption to chemisorption

Since the intermediate step for H_2 formation in the ISM involves a H atom adsorbed on a carbonaceous substrate, an interesting process to model is the transition between the two different adsorption states: physisorption and chemisorption, whose real potential is shown in Fig. 1.9.

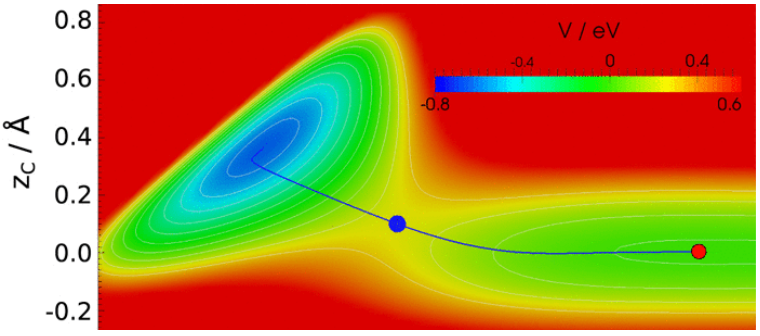

Figure 1.9: Real 2D potential for H adsorption on graphene [26].

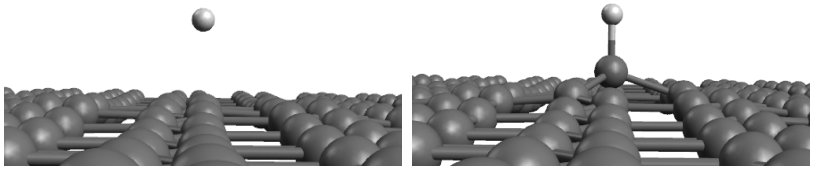

Figure 1.10: Left: H approaching the carbon surface (physisorption state). Right: bond formation due to carbon packering (chemisorption state).

Fig. 1.10 shows the surface behaviour in the two different adsorption states. When hydrogen is physisorbed on a graphitic surface, the sp^2 carbon hybridization is maintained, without losing the planar structure. In order to form a chemical bond with the H atom, the carbon involved needs to change its orbital hybridization into the sp^3, leading to a tetrahedral configuration. The surface rearrangement, i.e. the so called carbon *packering*, produces an energy barrier of ~ 0.2 eV.

In classical conditions, the hydrogen atom can move to the chemisorption well overcoming the barrier through thermal activation, but at extreme small temperature desorption is more likely. For temperature well below the adsorption barrier, adsorption can still occur via tunneling through the barrier while the desorption channel is closed. Thus, the phisisorbed hydrogen atom remains on the surface for a time long enough to react [8], i.e. to relax into the chemisorption well.

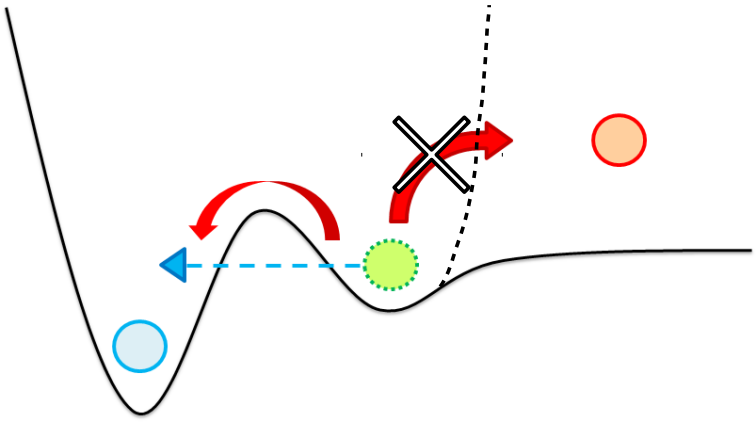

Figure 1.11: Schematic representation of classical and quantum mechanisms for the adsorption process.

Chapter 2

Theoretical background

In this chapter we present the theoretical background of this thesis work. In the first part we explain how to extrapolate the kinetic constant from a quantum dynamical calculation, introducing the concepts of *plateau time* and *correlation function*. In the second section we show how to build a discrete Hamiltonian equivalent to the continuum Langevin equation, and in the last part we treat an alternative and useful description of the environment.

2.1 From dynamics to kinetics

In order to illustrate the method exploited, we consider an isomerization reaction which admits a kinetics law like:

$$\frac{dP_B}{dt} = kP_A - k'P_B \tag{2.1}$$

where P_A and P_B are, respectively, the reagent and product populations, k is the rate constant for the direct reaction and k' for the reverse one. The time scale k^{-1} of a reaction is in general in the range of nanoseconds, too large for a quantum dynamics simulation. Fortunately, we do not need to follow the dynamics for such a (microscopically) long time, since a *kinetic regime* sets in on a much shorter time scale. This is the so called *plateau time* τ_P, beyond which Eq. 2.1 holds to a high accuracy. Since $\tau_P \ll k^{-1}$, it is reasonable to assume that P_A and P_B at this time are almost equal to their initial values, thus

$$P_A(t) \approx P_A(0) = 1 \quad \text{and} \quad P_B(t) \approx P_B(0) = 0 \tag{2.2}$$

In other words, τ_P is much smaller than the characteristic time in which we can see a macroscopic change in the population, and then Eq. 2.1 gives

$$\frac{dP_B}{dt}(t) \approx k \quad \text{for} \quad k^{-1} \gg t \geq \tau_P \tag{2.3}$$

In this way we do not need to perform the dynamics for the entire time necessary for the reaction to occur, but only up to the scale of τ_P, microscopically large but macroscopically small, beyond which the detailed dynamics converts to kinetics.

In the following paragraph we demonstrate that the rate constant can be calculated as the long-time limit of a canonical correlation function [23][27][28][29].

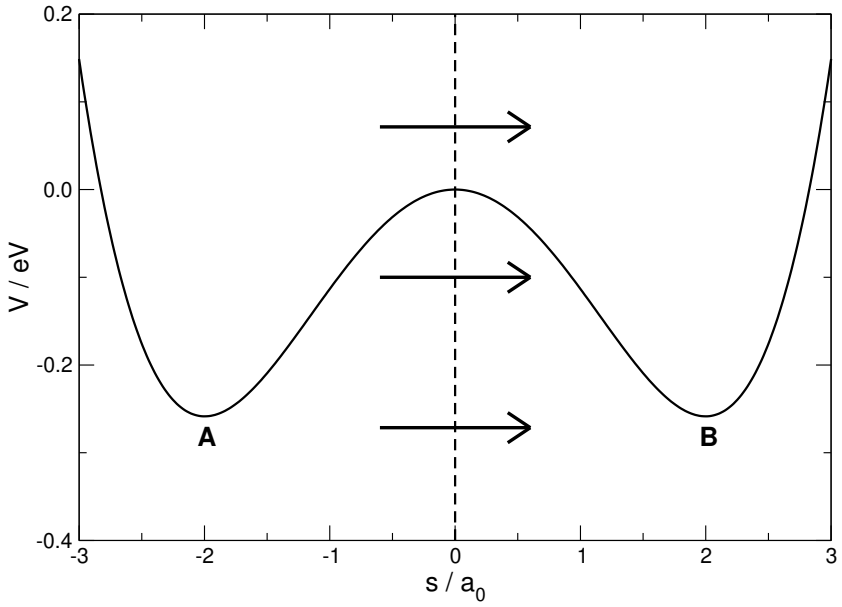

Figure 2.1: Schematic representation of the flux through the partition surface.

2.1.1 Correlation function expression

The kinetic constant in the τ_P scale can be written as the rate of product appearance:

$$k = \frac{dP_B}{dt} = \mathrm{Tr}\left[\frac{\partial \rho_0(t)}{\partial t} h\right] \tag{2.4}$$

where $\rho_0(t)$ is the statistic operator that describes the system initially in equilibrium in the reagent well ($P_A(0) = 1$), and h is a projector onto the product well. Thanks to the Liouville theorem in quantum regime for a generic statistic operator ρ:

$$\frac{d\rho}{dt} = \frac{\partial \rho}{\partial t} + \frac{i}{\hbar}[\mathcal{H}, \rho] = 0 \tag{2.5}$$

where $\hbar$ is the reduced Plank constant and $\mathcal{H}$ is the Hamiltonian operator, we obtain the Liouville von Newmann equation for our ρ_0:

$$\frac{\partial \rho_0}{\partial t} = -\frac{i}{\hbar}[\mathcal{H}, \rho_0] \tag{2.6}$$

In order to describe the reagents in equilibrium at a fixed temperature T, a reasonable expression for ρ_0 is

$$\rho_0 = \frac{e^{-\frac{\beta\mathcal{H}}{2}}(1-h)e^{-\frac{\beta\mathcal{H}}{2}}}{Z_A} \qquad \text{with } \beta = (k_B T)^{-1} \tag{2.7}$$

where β is the inverse temperature, k_B is the Boltzmann constant and $(1-h)$ is the projector onto the reagent state; Z_A is the partition function of the reagents, which provides the normalization of the statistic operator:

$$Z_A = \mathrm{Tr}\left[e^{-\beta\mathcal{H}}(1-h)\right] \tag{2.8}$$

We obtain the following expression for the product appearance rate:

$$\frac{dP_B}{dt} = \lim_{t\to\tau_P} -\frac{i}{\hbar}\mathrm{Tr}\left[e^{-\frac{\beta\mathcal{H}}{2}}[\mathcal{H},(h-1)]e^{-\frac{\beta\mathcal{H}}{2}}h(t)\right]\frac{1}{Z_A}$$

$$= \lim_{t\to\tau_P} \frac{i}{\hbar}\mathrm{Tr}\left[e^{-\frac{\beta\mathcal{H}}{2}}[\mathcal{H},h]e^{-\frac{\beta\mathcal{H}}{2}}h(t)\right]\frac{1}{Z_A} \tag{2.9}$$

It is possible to consider the time dependent variation of the product population as the flux through the surface that divides the reagents from the products (Fig. 2.1), introducing the flux operator F:

$$F = \frac{i}{\hbar}[\mathcal{H},h] \tag{2.10}$$

and its thermalized form F_β, the so-called Boltzmannized flux operator:

$$F_\beta = e^{-\frac{\beta\mathcal{H}}{2}}Fe^{-\frac{\beta\mathcal{H}}{2}} \tag{2.11}$$

Therefore, the rate constant takes the form

$$k = \lim_{t\to\tau_P}\frac{\mathrm{Tr}\big[F_\beta h(t)\big]}{Z_A} \tag{2.12}$$

Different types of correlation functions can be employed to calculate the kinetic constant, but in this case the one immediately applicable is the flux-side correlation function C_{fs}:

$$C_{fs}(t) = \mathrm{Tr}\big[F_\beta h(t)\big] \tag{2.13}$$

Alternatively, it is possible to use its time derivative expression, known as flux-flux correlation function C_{ff}:

$$C_{ff}(t) = \mathrm{Tr}\big[F_\beta F(t)\big] \tag{2.14}$$

Thus, the final expression for the rate reads as

$$k = \frac{1}{Z_A}\lim_{t\to\tau_P} C_{fs}(t) = \frac{1}{Z_A}\lim_{t\to\tau_P}\int_0^\infty dt\; C_{ff}(t) \tag{2.15}$$

2.2 Hamiltonian description

Real physical and chemical processes, like the ones described in the previous chapter, are characterized by the permanent interaction of the reactive species with the environment. Their coupling results in an irreversible energy transfer into the environment, which exerts a fluctuating force on the reactant system and breaks its coherent motion. Thus, the phenomena of *dissipation*, *fluctuation* and *coherence* must be well modeled.

When quantum effects become important, e.g. for light atoms and/or low temperatures, the system typically is strongly coupled to at least a part of its environment. The coupling terms and the frequencies of the environment are related to the spectral density $J(\omega)$ (Fig. 2.2), which describes the coupling of the particle to its environment, and represents the key quantity that correlates fluctuation with dissipation [30] (as explained in the following section).

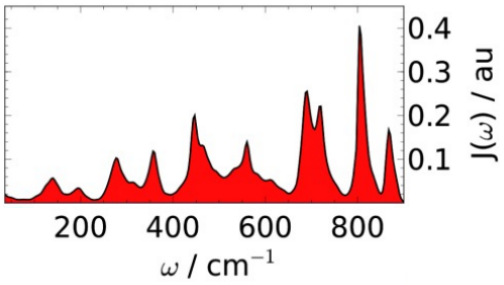

Figure 2.2: Graphene spectral density [30].

The Hamiltonian can be thought of as a normal mode expansion of the environment, assuming it is an ensemble of Harmonic Oscillators (HOs) (Fig. 2.3), since we are not interested in the chemical structure of the solvent, surface or substrate in general where the reaction occurs. Instead of describing all of the environment coordinates, it is possible to figure out, through $J(\omega)$, which oscillators are coupled more with the system and which less. Thus, we can have an equivalent description of the environment. This representation allows us to treat the fluctuating-dissipative forces that real systems experiences when in contact with their atomistic environment. In fact, for example, solvent rotations, protein vibrations or phonons can be assumed, in first approximation, as harmonic oscillators.

2.2.1 Generalized Langevin Equation

In a monodimensional potential $V(x)$ a particle's motion in a dissipative environment is well described by the Generalized Langevin Equation (GLE) [31]

$$F(t) = m\ddot{s} + \int_{-\infty}^{t} dt' \; \Gamma(t-t')\dot{s}(t') + \frac{\partial V(s)}{\partial s} \tag{2.16}$$

where $F(t)$ is the total force applied to the particle, m and s are respectively the mass and position of the particle, and $\Gamma(t-t')$ is the memory kernel. The stochastic force F, that presents effects on fluctuations, is closely related to the time dependent friction force $\Gamma(t)$, which affects the energy dissipation, by the classical fluctuation-dissipation theorem:

$$\langle F(t)F(0)\rangle = \frac{\Gamma(t)k_B T}{m} \tag{2.17}$$

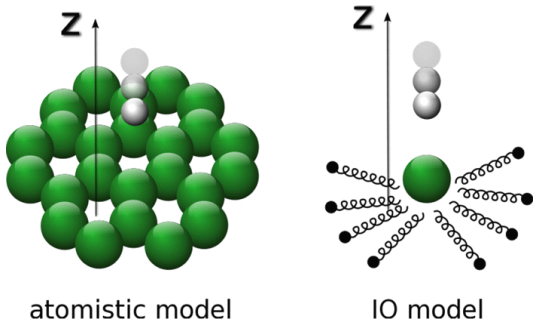

Figure 2.3: Schematic representation of the gas-graphene interaction [26].

where $\Gamma(t)$ is determined in turn by the spectral density defined by

$$J(\omega) = m\omega \mathrm{Re}\tilde{\Gamma}(\omega) \tag{2.18}$$

which is a real, odd function of the frequency ω. Here $\tilde{\Gamma}(\omega)$ is the Fourier transform of the memory kernel $\Gamma(t)$.

This kind of description is not consistent with quantization procedures and so it is not directly applicable for conducting quantum investigations. However, it can be demonstrated that a Hamiltonian equivalent to the Langevin equation exists and can then be used, under suitable conditions, to quantize particle motion in the standard setting.

2.2.2 Independent oscillator model

As shown in Fig. 2.4, in the Independent Oscillator (IO) model [33], also known as the Caldeira-Leggett model [34], the quantum particle, i.e. the system, is bilinearly coupled with each degree of freedom of the thermal bath, which in turn is harmonic and thus described by a harmonic oscillator Hamiltonian term. Thus, the global Hamiltonian $\mathcal{H}$ can be written as sum of two main contributions:

$$\mathcal{H} = \mathcal{H}_S + \mathcal{H}_{B(S)} \tag{2.19}$$

where $\mathcal{H}_S$ is the system Hamiltonian and $\mathcal{H}_{B(S)}$ is the bath Hamiltonian, which contains the system-bath coupling term [35][36]. More in detail, the Hamiltonian expression of such a setup is

$$\mathcal{H} = \frac{p^2}{2m} + V(s) + \sum_k \left[\frac{p_k^2}{2m_k} + \frac{1}{2} m_k \omega_k^2 \left(q_k - \frac{c_k s}{m_k \omega_k^2} \right)^2 \right] \tag{2.20}$$

where p is the momentum of the system and s is its coordinate, and p_k, m_k, ω_k, q_k and c_k respectively represent momentum, mass, frequency, position and coupling term of each k oscillator of the bath.

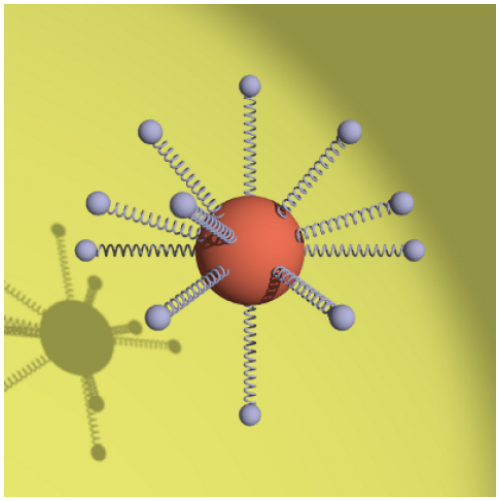

Figure 2.4: Schematic representation of system-bath coupling in the IO model [32].

The equivalence between this Hamiltonian and the GLE in Eq. 2.16 can be proved by the classical derivation that follows. A similar development is possible in the quantum setting for Heisenberg picture operators, with the due care needed for accounting the non-commutatitivy of the operators.

The classical equations of motion of Eq. 2.20 for the system degree of freedom read as

$$\dot{s} = \{s, \mathcal{H}\} = \frac{p}{m} \tag{2.21}$$

$$\dot{p} = \{p, \mathcal{H}\} = -\frac{\partial V(s)}{\partial s} + \sum_k \left(c_k q_k - \frac{c_k^2}{m_k \omega_k^2} s \right) \tag{2.22}$$

and the ones for each DOF of the bath are given by

$$\dot{q_k} = \{q_k, \mathcal{H}\} = \frac{p_k}{m_k} \tag{2.23}$$

$$\dot{p_k} = \{p_k, \mathcal{H}\} = -m_k \omega_k^2 q_k + c_k s \tag{2.24}$$

From these two pairs of Heisenberg derivatives it is possible to obtain a second order differential equation both for the system and the bath coordinate:

$$m\ddot{s} = -\frac{\partial V(s)}{\partial s} + \sum_k \left(c_k q_k - \frac{c_k^2}{m_k \omega_k^2} s \right) \tag{2.25}$$

$$m_k \ddot{q_k} = -m_k \omega_k^2 q_k + c_k s \tag{2.26}$$

In order to solve the equation for the dynamics of the system $s(t)$, we have first to obtain the dynamics of each DOF of the bath. We consider the initial time t_0 for which we have $\{q_k^0, p_k^0\}$, obtaining

$$q_k(t) = \frac{c_k}{m_k \omega_k^2} s(t) + \left[q_k^0 - \frac{c_k}{m_k \omega^2} s(t_0) \right] cos(\omega(t - t_0)) + \\ + \frac{p_k^0}{m_k \omega_k} sin(\omega_k(t - t_0)) - \frac{c_k}{m_k \omega_k^2} \int_{t_0}^{t} cos(\omega_k(t - t')) \dot{s}(t') dt' \tag{2.27}$$

At this point we can substitute the solution for q_k into Eq. 2.25:

$$m\ddot{s} = -\frac{\partial V(s)}{\partial s} + \sum_k \left\{ c_k \left[q_k^0 - \frac{c_k}{m_k \omega_k^2} s(t_0) \right] cos(\omega_k(t - t_0)) + \right. \\ \left. + \frac{p_k^0}{m_k \omega_k} sin(\omega_k(t - t_0)) - \int_{t_0}^{t} \frac{c_k}{m_k \omega_k} cos(\omega_k(t - t')) \dot{s}(t') dt' \right\} \tag{2.28}$$

Taking the limit of $t_0 \to -\infty$ we obtain the total force applied to the system particle that appear in the GLE

$$F(t) = \sum_k \left\{ c_k \left[q_k^0 - \frac{c_k}{m_k \omega_k^2} s(t_0) \right] cos(\omega_k(t - t_0)) + \frac{p_k^0}{m_k \omega_k} sin(\omega_k(t - t_0)) \right\} \tag{2.29}$$

and the memory kernel

$$\Gamma(t-t') = \frac{1}{m}\sum_k \frac{c_k}{m_k\omega_k} cos(\omega_k(t-t')) \tag{2.30}$$

demonstrating that the IO Hamiltonian is equivalent to the GLE, with a spectral density J_{IO} characterized by

$$J_{\mathrm{IO}}(\omega) = \frac{\pi}{2}\sum_k \frac{c_k^2}{m_k\omega_k}\delta(\omega-\omega_k) \tag{2.31}$$

It is now possible to prove that this J_{IO} can reproduce any spectral density, with the general expression

$$J(\omega) = \int d\omega' J(\omega')\delta(\omega-\omega') \tag{2.32}$$

considering a uniform discretization of the frequencies ($\omega_k = k\Delta\omega$):

$$J(\omega) \simeq \sum_k \Delta\omega J(\omega_k)\delta(\omega-\omega_k) \tag{2.33}$$

It follows that

$$\Delta\omega J(\omega_k) = \frac{\pi}{2}\frac{c_k^2}{m_k\omega_k} \tag{2.34}$$

which means we have found the value of each coupling coefficient c_k that reproduces the correct spectral density at any frequency:

$$c_k = \sqrt{\frac{2m_k\omega_k\Delta\omega J(\omega_k)}{\pi}} \tag{2.35}$$

The transformation to a finite and discrete representation of the bath, necessary for a computational investigation, narrows the time range where the strict equivalence between the GLE and the Hamiltonian holds. The frequency discretization leads to the upper limit called *Poincaré recurrence time*

$$t_{rec} = \frac{2\pi}{\Delta\omega} \tag{2.36}$$

beyond which the energy dissipated into the bath recurs to the system. The lower limit δt, our time step, depends instead on the finite number N of HOs used, i.e. on the maximum frequency value we can consider, the *frequency cutoff* $\omega_c = N\Delta\omega$:

$$\delta t = \frac{2\pi}{\omega_c} \tag{2.37}$$

2.3 Effective modes

As introduced in the previous chapter, we have to build a finite bath to perform the dynamics. The number of HOs we choose affects the computational cost on one hand, and the accuracy of the description on the other. In order to optimize the number of HOs without losing accuracy, we can try to identify the collective

modes that, in the given time window of interest, are most effective in coupling the system to the environment. One intriguing possibility is with the help of the so-called *effective modes* [37][38][39].

In order to bring the bath into the effective mode representation, with new coordinates, frequencies and coupling term that bound the system with each HO, we have first to reformulate the Hamiltonian in Eq. 2.20, considering the new mass-weighted bath modes $x_k = m_k q_k$ ($p_k = \dot{x_k}$):

$$\mathcal{H} = \underbrace{\frac{p^2}{2m} + V(x)}_{\mathcal{H}_S^{(0)}} + \underbrace{\frac{1}{2}\sum_k \left[p_k^2 + \omega_k^2 x_k^2\right]}_{\mathcal{H}_B^{(0)}} + \underbrace{\sum_k -c_k x_k s}_{\mathcal{H}_{int}^{(0)}} + \underbrace{\frac{1}{2}\sum_k \frac{c_k^2}{\omega_k^2} s^2}_{\Delta V}$$

where we now identify $\mathcal{H}_S$ and $\mathcal{H}_B$ respectively as the pure system Hamiltonian and the pure bath Hamiltonian (kinetic energy + potential), $\mathcal{H}_{int}$ as the system-bath interaction Hamiltonian and ΔV is the renormalization potential. The latter is the so-called *counter term*, which guarantees that the classical potential of mean force is not distorted by the bath and that the ground-state of the overall system is bounded from below when the system potential is bound from below.

Upon introducing the renormalization frequency $\delta\Omega$, the latter can be recast in the form

$$\Delta V = \frac{1}{2} m \delta\Omega^2 s^2 \tag{2.38}$$

that explicitly shows that renormalization is a harmonic correction. Here

$$\delta\Omega^2 = \frac{1}{m}\sum_k \frac{c_k^2}{\omega_k^2} \tag{2.39}$$

which in the continuum limit (see Eq. 2.34) corresponds to

$$\delta\Omega^2 = \frac{1}{m}\frac{2}{\pi}\int_0^\infty d\omega \frac{J(\omega)}{\omega} \tag{2.40}$$

In order to treat the HO parameters, we consider the sum over all bath modes of the coupling coefficients squared, starting from Eq. 2.35:

$$\sum_k c_k^2 = \frac{2}{\pi}\sum_k \omega_k \Delta\omega J(\omega_k) \tag{2.41}$$

and we introduce a general coupling coefficient D_0 for which

$$D_0^2 = \sum_k c_k^2 \tag{2.42}$$

that in the continuum limit corresponds to

$$D_0^2 = \frac{2}{\pi}\int_0^\infty d\omega J(\omega)\omega \tag{2.43}$$

We define a normalized coupling term as

$$\tilde{c}_k = \frac{c_k}{D_0} \tag{2.44}$$

that allows us to build the first effective mode coordinate X_1:

$$X_1 = \sum_k \tilde{c}_k x_k \tag{2.45}$$

and the first effective mode frequency:

$$\Omega_1^2 = \sum_k \tilde{c}_k^2 \omega_k^2 \tag{2.46}$$

that in the continuum limit can be expressed as

$$\Omega_1^2 = \frac{\int_0^\infty d\omega J(\omega)\omega^3}{\int_0^\infty d\omega J(\omega)\omega} \tag{2.47}$$

In this way we obtain a new expression for the interaction Hamiltonian of the first normal mode:

$$\mathcal{H}_{int}^{(0)} = -D_0 X_1 x \tag{2.48}$$

and for its potential:

$$V(X_1) = \frac{1}{2}\Omega_1^2 X_1^2 \tag{2.49}$$

Clarified how to build the first mode, we introduce a general orthogonal transformation $\mathbf{T}$ for which

$$\mathbf{X} = \mathbf{T}^t\mathbf{x} \qquad \text{and} \qquad \mathbf{\Omega}^2 = (\mathbf{T}^t)^2\mathbf{w}^2 \tag{2.50}$$

where $\mathbf{X}$ and $\mathbf{\Omega}$ are the vector respectively of the effective modes and the frequencies associated, $\mathbf{X}^t = (X_1, X_2, ..., X_N)$ and $\mathbf{\Omega}^t = (\Omega_1, \Omega_2, ..., \Omega_N)$, while $\mathbf{x}$ and $\mathbf{w}$ are respectively the vector of the old coordinates and the old frequencies, $\mathbf{x}^t = (x_1, x_2, ..., x_N)$ and $\mathbf{w}^t = (\omega_1, \omega_2, ..., \omega_N)$, and defined in such a way that

$$X_i = \sum_{k=1}^{N} (\mathbf{T}^t)_{ik} x_k = \sum_{k=1}^{N} \mathbf{T}_{ki} x_k \qquad \text{and} \qquad \Omega_i^2 = \sum_{k=1}^{N} (\mathbf{T}^t)_{ik}^2 \omega_k^2 = \sum_{k=1}^{N} \mathbf{T}_{ki}^2 \omega_k^2 \tag{2.51}$$

The matrix $\mathbf{T} = [\mathbf{t_1 t_2 t_3 ... t_N}]$ is required to contain the normalized coefficients c_k in the first column $\mathbf{t_1}$, but is otherwise an arbitrary orthogonal transformation. Thus, the vector containing the first column elements is entirely determined by $J(\omega)$ and spans the *effective mode space*, while $\mathbf{t_2}, \mathbf{t_3}, ..., \mathbf{t_N}$ span the *residual space*.

If we rewrite the bath Hamiltonian with a matrix formalism, we have:

$$\mathcal{H}_B^{(0)} = \frac{1}{2}(\mathbf{p}^t\mathbf{p} + \mathbf{x}^t\mathbf{v}\mathbf{x}) = \frac{1}{2}(\mathbf{P}^t\mathbf{P} + \mathbf{X}^t\mathbf{V}\mathbf{X}) \tag{2.52}$$

where $\mathbf{p}$ and $\mathbf{P} = \mathbf{T}^t\mathbf{p}$, $\mathbf{p}^t = (p_1, p_2, ..., p_N)$ and $\mathbf{P}^t = (P_1, P_2, ..., P_N)$, are respectively the old and transformed momentum vector, $\mathbf{v}_{ki} = \delta_{ki}\omega_k^2$ is the potential matrix and $\mathbf{V} = \mathbf{T}^t\mathbf{v}\mathbf{T}$ is the transformed potential matrix, with

$$\mathbf{V}_{ij} = \sum_{k=1}^{N} (\mathbf{T}^t)_{ik}\omega_k^2 \mathbf{T}_{kj} = \sum_{k=1}^{N} \omega_k^2 (\mathbf{t_i})_k (\mathbf{t_j})_k \qquad \text{and} \qquad \mathbf{V}_{1k} = \mathbf{V}_{k1} = d_k \tag{2.53}$$

and the bath Hamiltonian can be rewritten as

$$\mathcal{H}_B^{(0)} = \frac{1}{2}\left(P_1^2 + \Omega_1^2 X_1^2\right) + \frac{1}{2}\left[\sum_{k=2}^{N} P_k^2 + \sum_{k,l=2}^{N} X_k V_{kl} X_l\right] + \sum_{k=2}^{N} d_k X_1 X_k \tag{2.54}$$

In order to define the spectral density felt by the effective mode X_1, we have now to treat the normal modes of the $(N-1)$-dimensional residual bath $\bar{\mathbf{X}}$ described by $\bar{\mathbf{X}}^t = (X_2, X_3, ..., X_N)$, introducing the potential matrix $\bar{\mathbf{V}}$ $(N-1)\times(N-1)$-dimensional for which $\bar{\mathbf{V}}_{ij} = \mathbf{V}_{i,j}$ for $k = 2, 3, ..., N$. The Hamiltonian can be rewritten as

$$\mathcal{H}_B^{(0)} = \frac{1}{2}\left(P_1^2 + \Omega_1^2 X_1^2\right) + \frac{1}{2}\left[\mathbf{P}^t\mathbf{P} + \bar{\mathbf{X}}^t\bar{\mathbf{V}}\bar{\mathbf{X}}\right] + \sum_{k=2}^{N} d_k X_1 \bar{\mathbf{X}}_k \tag{2.55}$$

We introduce a orthogonal matrix $\mathbf{U}$ that allows to diagonalize $\bar{\mathbf{V}}$ ($\mathbf{U}\bar{\mathbf{V}} = \bar{\mathbf{V}}_D$), thanks to which we have

$$\bar{\mathbf{X}}^t\bar{\mathbf{V}}\bar{\mathbf{X}} = \bar{\mathbf{X}}^t\mathbf{U}\bar{\mathbf{V}}_D\mathbf{U}^t\bar{\mathbf{X}} = \mathbf{Q}^t\bar{\mathbf{V}}_D\mathbf{Q} \tag{2.56}$$

eventually obtaining

$$\sum_{k=2}^{N} d_k(\bar{\mathbf{X}})_k = -\sum_{j=2}^{N} C_j Q_j \tag{2.57}$$

where the new coupling term corresponds to

$$C_j = -\sum_{k=2}^{N} d_k U_{kj} \tag{2.58}$$

It follows that the new expression for the bath Hamiltonian

$$\mathcal{H}_B^{(0)} = \underbrace{\frac{1}{2}\left(P_1^2 + \Omega_1^2 X_1^2\right)}_{\mathcal{H}_S^{(1)}} + \underbrace{\frac{1}{2}\sum_{k=2}^{N}\left[P_k^2 + \Omega_k^2 Q_k^2\right]}_{\mathcal{H}_B^{(1)}} + \underbrace{\sum_{k=2}^{N} -C_k X_k X_1}_{\mathcal{H}_{int}^{(1)}} \tag{2.59}$$

corresponds to a Hamiltonian of one effective mode coupled to a $(N-1)$-dimensional bath. Hence, the X_1 behavior is ruled by a Langevin dynamics characterized by the new spectral density

$$J_1(\omega) = \frac{\pi}{2}\sum_{k=2}^{N}\frac{C_k^2}{\Omega_k}\delta(\omega - \Omega_k) \tag{2.60}$$

In order to obtain a perfect parallelism with the Hamiltonian in Eq. 2.20, we have to renormalize the effective mode frequency:

$$\Omega_{1,ren}^2 = \Omega_1^2 - \delta\Omega_1^2 \tag{2.61}$$

where

$$\delta\Omega_{1,ren}^2 = \sum_{k=2}^{N}\frac{C_k^2}{\Omega_k^2} \tag{2.62}$$

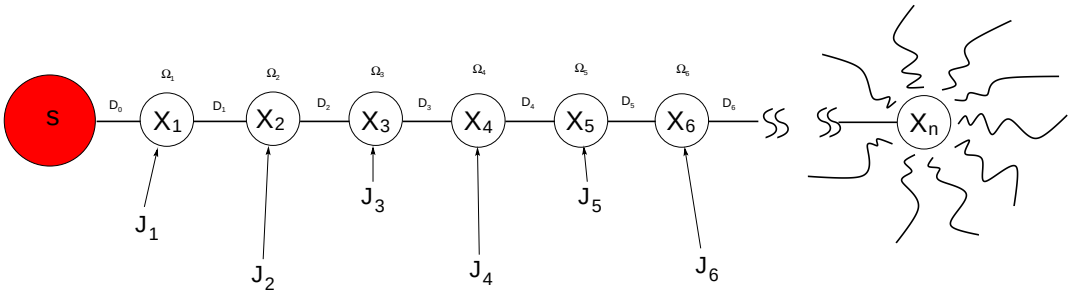

Figure 2.5: Effective mode chain coupled with the system and the residual bath [41].

that in the continuum limit reads

$$\delta\Omega_{1,ren}^2 = \frac{2}{\pi}\int_0^\infty d\omega \frac{J_1(\omega)}{\omega} \tag{2.63}$$

In this way we can adopt a Langevin description of the bath Hamiltonian:

$$\mathcal{H}_B^{(0)} = \frac{P^2}{2} + \frac{\Omega_{1,ren}^2 X_1^2}{2} + \sum_{k=2}^{N}\left[\frac{P_k^2}{2} + \frac{1}{2}\Omega_k^2\left(Q_k - \frac{C_k X_1}{\Omega_k^2}\right)^2\right] \tag{2.64}$$

If we iterate this procedure, we obtain the chain structure of effective modes shown in Fig. 2.5, coupled at one extremity to the system and at the other to the residual bath. Indeed, for each $J_n(\omega)$ we can introduce a new effective mode X_{n+1} with its frequency, and we obtain a new spectral density $J_{n+1}(\omega)$ that couples the new mode to the residual bath [40]. It can be shown that the coupling to the residual bath in the infinitely long chain limit corresponds to the so-called Rubin model of dissipation describing a quasi-Ohmic behaviour [41].

In practical calculations, one definite advantage of using such a representation is that we can truncate the chain and reproduce the short-time dynamics rather accurately, when the main issue is the propagation of excitation from the system to the bath (in general, truncated chains reproduce exactly the memory kernel, for times that become increasingly longer when increasing the chain length) [42].

In our test calculations (to be described in Chapter 7) we use truncated effective mode chains to obtain optimal representations of the bath in normal form. Specifically, upon truncating the chain after N effective modes have been introduced, we perform a transformation back into the normal form. This then generates a set of frequencies and coupling coefficients which is optimal for the given spectral density, in the sense that it describes precisely the same dynamics of the effective chain N modes long but now with a N-dimensional bath in normal form. This transformation into normal representation allows us to exploit the properties of the effective mode chain, while keeping the bath in a form which is yet simple and for which real-time propagation is relatively straightforward (differently from what happens with the bath in a linear chain form).

Chapter 3

Method

In this chapter we explain the methodology used to obtain the numerically exact evaluation of the chemical rate constant from full quantum dynamical calculations.

The first step of our strategy consists in sampling the initial state of the thermal bath at a given temperature T. For each sampled bath state we performed the dynamics, both in imaginary and real time, of the system+bath ensemble, exploiting the ML-MCTDH method. Averaging the results of these quantum dynamical simulations allows us to compute the rate constant k at each temperature of interest.

At the end of our simulations we compared this kinetic constant, k, with the kinetic constant arising from the classical (one-dimensional) *Transition State Theory* (TST):

$$k_{\mathrm{TST},cl} = \frac{1}{2\pi\hbar\beta}\frac{e^{-\beta E_b}}{Z_{r,cl}} \tag{3.1}$$

where $Z_{r,cl}$ is the classical partition function of the reagents. In this way we obtained a measure of the contribution of the quantum effect, the so-called transmission coefficient κ, defined here as

$$\kappa(T) = \frac{k(T)}{k_{\mathrm{TST,cl}}(T)} \tag{3.2}$$

Conventional *Time-Dependent Wave-Packet* (TDWP) techniques succeed in giving reaction probabilities at 0 K only. For finite temperatures, we would need to compute a thermal average after the dynamical performance. With our approach, instead, we can directly obtain rate constants at a given temperature.

3.1 Wave-packet expression of C_{fs} and Z_A

Both C_{fs} and Z_A, introduced in Section 2.1, can be computed involving a sum over the high-dimensional states $|I\rangle$

$$C_{fs}(t) = \sum_I \langle I|F_\beta h(t)|I\rangle \tag{3.3}$$

$$Z_A = \sum_I \langle I|e^{-\beta\mathcal{H}}(1-h)|I\rangle \tag{3.4}$$

Since the total Hamiltonian is the sum of two different contributions, one arising from the system and one from the bath, each $|I\rangle$ state can be written in a product form:

$$|I\rangle = |\nu, N\rangle \tag{3.5}$$

where $|\nu\rangle$ is a system state and $|N\rangle$ is a bath state.

In a system-bath set-up F is the system-only flux operator and has the following spectral representation:

$$F = \sum_j \nu_j \, |\nu_j\rangle\langle\nu_j| \tag{3.6}$$

where each $|\nu_j\rangle$ is an eigenvector of the system-only flux operator and ν_j is its respective eigenvalue. We introduce the Boltzmann operator $e^{-\frac{\beta\mathcal{H}_S}{2}}$ in the F expression as follows:

$$F = e^{\frac{\beta\mathcal{H}_S}{2}} e^{-\frac{\beta\mathcal{H}_S}{2}} F e^{-\frac{\beta\mathcal{H}_S}{2}} e^{\frac{\beta\mathcal{H}_S}{2}} = e^{\frac{\beta\mathcal{H}_S}{2}} F_\beta^S \; e^{\frac{\beta\mathcal{H}_S}{2}} \tag{3.7}$$

where the F_β^S is the system-only boltzmannized flux operator, a compact form of the flux operator that kills every eigenvector but the relevant ones at the temperature fixed by β. The spectral resolution of F_β^S is of low rank, meaning that it contains few non-vanishingly-small eigenvalues

$$F_\beta^S = \sum_j \nu_j^\beta |\nu_j^\beta\rangle\langle\nu_j^\beta| \tag{3.8}$$

and thus the system+bath boltzmannized flux operator now reads as

$$F_\beta = e^{-\frac{\beta\mathcal{H}}{2}} e^{\frac{\beta\mathcal{H}_S}{2}} F_\beta^S \; e^{\frac{\beta\mathcal{H}_S}{2}} e^{-\frac{\beta\mathcal{H}}{2}} = \sum_{j,N} \nu_j^\beta e^{-\frac{\beta\mathcal{H}}{2}} e^{\frac{\beta\mathcal{H}_S}{2}} |\nu_j^\beta, N\rangle\langle\nu_j^\beta, N| e^{-\frac{\beta\mathcal{H}}{2}} e^{\frac{\beta\mathcal{H}_S}{2}}$$

By replacing this expression in Eq. 3.3 we obtain

$$\begin{aligned} C_{fs} &= \sum_I \sum_{j,N} \nu_j^\beta \langle I| e^{-\frac{\beta\mathcal{H}}{2}} e^{\frac{\beta\mathcal{H}_S}{2}} |\nu_j^\beta, N\rangle\langle\nu_j^\beta, N| e^{\frac{\beta\mathcal{H}_S}{2}} e^{-\frac{\beta\mathcal{H}}{2}} h(t)|I\rangle \\ &= \sum_{j,N} \nu_j^\beta \langle\nu_j^\beta, N| e^{\frac{\beta\mathcal{H}_S}{2}} e^{-\frac{\beta\mathcal{H}}{2}} h(t) e^{-\frac{\beta\mathcal{H}}{2}} e^{\frac{\beta\mathcal{H}_S}{2}} |\nu_j^\beta, N\rangle \\ &= \sum_{j,N} \nu_j^\beta \langle\phi_{j,N}^\beta| e^{-\frac{\beta H}{2}} h(t) e^{-\frac{\beta H}{2}} |\phi_{j,N}^\beta\rangle \end{aligned} \tag{3.9}$$

where $|\phi_{j,N}^\beta\rangle$ is the product of a system function $\Phi_{\beta,j}(s)$ and a bath one $\Phi_N(q_1, q_2, ..., q_N)$, re-projected onto the system+bath Hamiltonian space applying the anti Boltzmann operator:

$$|\phi_{j,N}^\beta\rangle = |\bar{\nu}_j, N\rangle = e^{\frac{\beta\mathcal{H}_S}{2}} |\nu_j^\beta, N\rangle$$

In this way we obtain the initial representation of the system states, but only for the relevant ones, reducing the trace calculation to the dynamics of a few independent packets: a couple of system states times a few hundreds realization of the thermal bath state.

Once we have built the initial wave-packet $\phi_{j,N}^\beta$ we relax it for a time $\beta/2 = (2k_BT)^{-1}$ (that is, we perform an imaginary time propagation) and then evolve the resulting

wave-packet for a sufficiently long (real) time. The expectation value of the Heaviside step function is computed along the dynamics and the correlation function computed as outlined above. Therefore, the final compact expression of the flux-side correlation function is

$$C_{fs} = \sum_{j,N} \nu_j^\beta \langle \phi_{j,N}^\beta | V_\beta^\dagger h V_\beta | \phi_{j,N}^\beta \rangle \tag{3.10}$$

where $V_\beta(t)$ is a propagator in complex time, $t - i\hbar\beta/2$.

For the partition function of the reagents the procedure is analogous, but no real time propagation is needed, and the expectation value of interest is the reagent projector.

3.2 Monte Carlo sampling

At a finite temperature we can have infinite possible configuration of the initial bath state, i.e. different distributions of HO excitations. If we rewrite Eq. 3.9 as

$$C_{fs} = Z_{bath} \sum_{j,N} \nu_j^\beta \ \frac{1}{Z_{bath}} e^{-\beta E_N} \langle \phi_{j,N}^\beta | e^{-\frac{\beta \mathcal{H}}{2}} h(t) e^{-\frac{\beta \mathcal{H}}{2}} | \phi_{j,N}^\beta \rangle e^{\beta E_N} \tag{3.11}$$

where Z_{bath} is the partition function of the bath and E_N is the energy of the configuration N, the correlation function can be expressed as a Boltzmann average:

$$C_{fs} = Z_{bath} \sum_j \langle \langle \nu_j^\beta W_{jN}^\beta \langle h(t) \rangle_{jN}^\beta \rangle \rangle_\beta \tag{3.12}$$

where W_{jN} is a thermal factor. In this way we reduce the sum up to infinity considering just the initial bath states complying with the Boltzmann distribution:

$$N \ \rightsquigarrow \ e^{-\beta E_N} \tag{3.13}$$

Since the bath is characterized by independent harmonic oscillators, each bath mode level n_i must comply with the Boltzmann distribution:

$$n_i \ \rightsquigarrow \ e^{-\beta \hbar \omega n_i} \tag{3.14}$$

To this end, we select the maximum occupied energy level of each mode using the Monte Carlo sampling for the initial bath state [43][44].

Using the same mathematical scheme we obtain an analogous expression for the partition function.

3.3 Wave-packet evolution

The propagation of our system+bath wave-packet is computed using the *MultiConfiguration Time-Dependent Hartree* (MCTDH) method, a general algorithm to solve the Time-Dependent Schrödinger Equation (TDSE) for multi-dimensional dynamical systems consisting of distinguishable particles [45][46].

Standard quantum investigations involve Time Dependent Wave-Packet (TDWP) approaches and have strong limitations in the number of DOFs considerable, because of the exponential scaling of the computational cost. MCTDH can determine the motion of the nuclei of a molecular system evolving on one or several coupled electronic potential energy surfaces, and is designed for treating multi-dimensional problems and considerably alleviating the above mentioned exponential scaling problem.

The Heidelberg MCTDH package consists in a set of programs for multidimensional quantum dynamics [47] that implements the most recent developments of the MCTDH theory and the Multi Layer (ML) variant that exploits a natural hierarchical construction for the wave function.

3.3.1 From TDH to ML-MCTDH

Standard quantum dynamics methods express the D-dimensional wavefunction $\Psi(t)$ as time independent primitive basis functions $\chi(q_i)$, such as the Discrete Variable Representation (DVR), weighted by time dependent coefficients $A(t)$:

$$\Psi(q_1 \cdots q_D, t) = \sum_{j_1=1}^{b_1} \cdots \sum_{j_D=1}^{b_D} A_{j_1,\cdots,j_D}(t) \chi_{j_1}^{(1)}(q_1) \cdots \chi_{j_D}^{(D)}(q_D) \tag{3.15}$$

where b_i is the number of basis functions chosen for the i-th DOF q. With this approach both the memory requirement and the computational cost exponentially increase with the number of DOFs, leading to the so called "dimensionality curse": considering the same number of basis functions for each DOF, $b_1 = \cdots = b_D = b$, a number of floating point operations equal to bD^{D+1} needs to be computed to solve the equation of motion.

A first step toward the solution for the exponential scaling problem is the *Time Dependent Hartree* (TDH), which represents the wave function as the product of *Single-Particle Functions* (SPFs) $\Phi(t)$ of each degree of freedom:

$$\Psi(t) = A(t)\Phi_1(t)\Phi_2(t) \cdots \Phi_D(t) \tag{3.16}$$

where each SPF evolves in order to furnish the best description of the system in approximation, determined through the variational principle. This approach presents a linear scaling of the computational cost with the number of DOFs, but is not able to describe the correlation within each DOF.

In order to overcome this problem, the MCTDH theory has been developed. It consists in representing each degree of freedom q as a multiconfigurational product of SPFs:

$$\Psi(q_1 \cdots q_D, t) = \sum_{j_1=1}^{b_1} \cdots \sum_{j_D=1}^{b_D} A_{j_1,\cdots,j_D}(t) \Phi_{j_1}^{(1)}(q_1, t) \cdots \Phi_{j_D}^{(D)}(q_D, t) \tag{3.17}$$

Moreover, it is possible to combine d_i monodimensional degrees of freedom q into a d_i-dimensional variable Q_i, so that the wave function reads as

$$\Psi(Q_1 \cdots Q_f, t) = \sum_{j_1=1}^{B_1} \cdots \sum_{j_f=1}^{B_f} A_{j_1,\cdots,j_f}(t) \Phi_{j_1}^{(1)}(Q_1, t) \cdots \Phi_{j_f}^{(f)}(Q_f, t) \tag{3.18}$$

where each B_i forms the new basis set for f new variables. In this method, called *mode combination*, the key point for the computational effort relief is the single particle function definition. In the basic version of MCTDH each SPF is expressed in terms of a time dependent coefficient $c(t)$ and a time independent basis function $u_i(Q_i)$:

$$\Phi(Q_i,t) = \sum_{\kappa} c_\kappa(t) u_i^{(\kappa)}(Q_i) \tag{3.19}$$

In the Multi Layer extension, the ML-MCTDH, each SPF is expressed as a multi-configurational product [48] and we can develop Eq. 3.17 as follows:

$$\begin{aligned}
|\Psi(t)\rangle &= \sum_{j_1}\cdots\sum_{j_D} A_{j_1,\cdots,j_D}(t)\prod_{\alpha=1}^{D}|\Phi_{j_\alpha}^{(\alpha)}(t)\rangle \\
|\Phi_{j_\alpha}^{(\alpha)}(t)\rangle &= \sum_{k_1}\cdots\sum_{k_{P(\alpha)}} B^{\alpha,j_\alpha}_{k_1,\cdots,k_{P(\alpha)}}(t)\prod_{\beta=1}^{P(\alpha)}|\varphi_{k_\beta}^{(\alpha,\beta)}(t)\rangle \\
|\varphi_{k_\beta}^{(\alpha,\beta)}(t)\rangle &= \sum_{l_1}\cdots\sum_{l_{M(\alpha,\beta)}} C^{\alpha,\beta,k_\beta}_{l_1,\cdots,l_{M(\alpha,\beta)}}(t)\prod_{\gamma=1}^{M(\alpha,\beta)}|\xi_{l_\gamma}^{(\alpha,\beta,\gamma)}(t)\rangle \\
&\cdots
\end{aligned} \tag{3.20}$$

We can iterate the expansion several times, expressing the last layer again as the product of a time dependent coefficient and a time independent basis function The wave function assumes a tree-like structure which can have different shape, as schematized in Fig. 3.1.

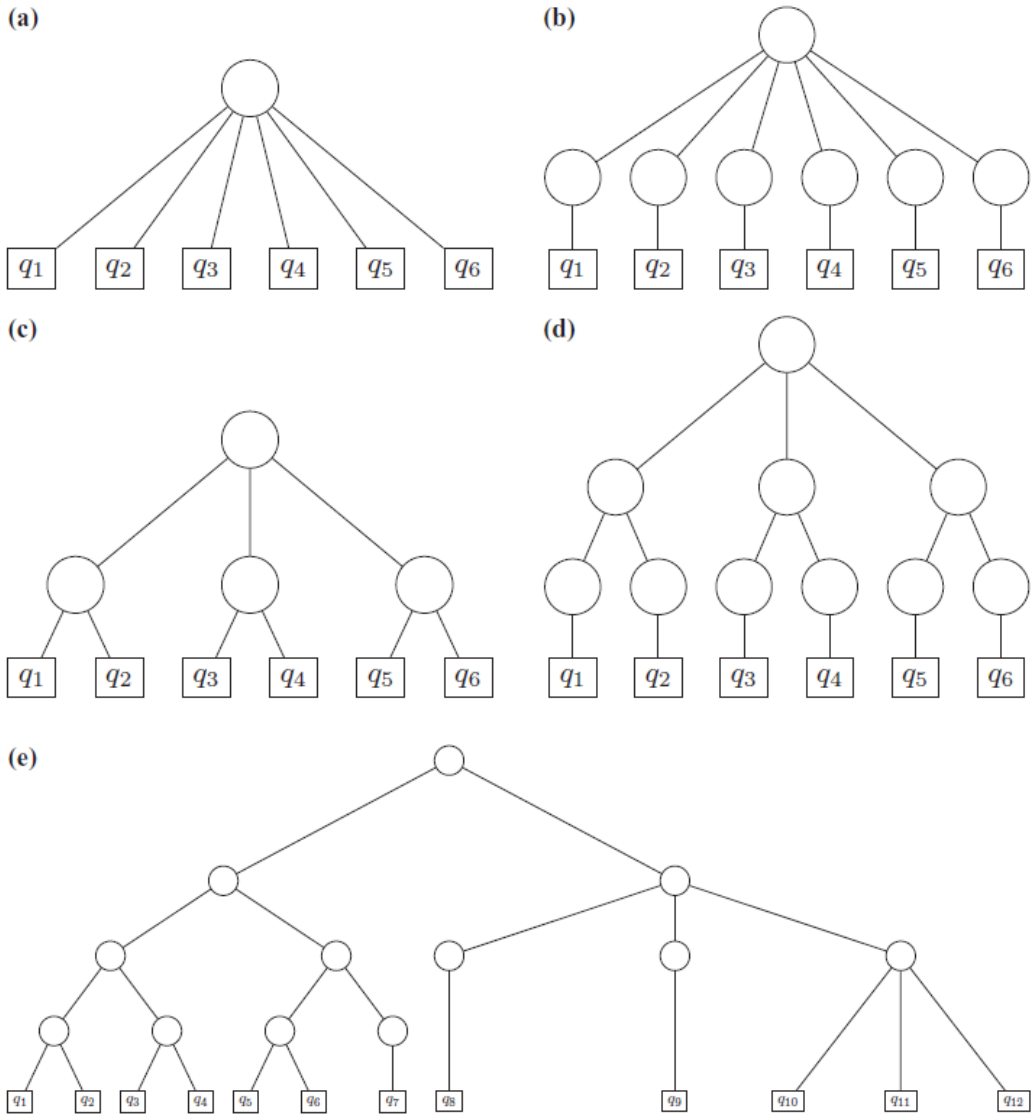

Figure 3.1: Possible bath structures. (a) Standard methods: the wave function is directly expanded into a primitive time-independent basis. (b) MCTDH: the wave function is first expanded into a basis of SPFs, which, in turn, are expanded onto a primitive basis. (c) MCTDH with mode combinations: the SPFs are expanded in two-dimensional primitive basis sets. (d) ML-MCTDH: the SPFs of the second layer are expanded into SPFs of the third layer which in turn are expanded into the primitive basis. (e) ML-MCTDH wave function tree with three and four layers and with mode combination [49].

Chapter 4

Coherent tunneling

In the first part of this PhD project we focused on the paradigmatic problem of a monodimensional symmetric Double Well (DW) potential coupled to a heat bath, a well known model system explored in detail in the literature. More specifically, we applied the procedure described in the previous chapters to a 1D+bath set-up investigated long ago by Topaler and Makri with the *QUasiAdiabatic propagator Path Integral* (QUAPI) [50] in their seminal work. We considered their DW1 potential, which is the most appropriate model for the description of a solid-state process, and we investigated the transition of the dynamics to kinetics in a wide range of physical parameters of the problem, namely the *temperature* and the *friction coefficient*. The latter subsumes the coupling to the bath, here assumed to be *quasi*-Ohmic.

Table 4.1: DW1 parameters in cm^{-1} (system and bath).

$E_b = 2085$	$\omega_m = 707$	$\omega_b = 500$	$\omega_c = 500$

4.1 Model potential

The symmetric DW potential felt by the system coordinate s is given by

$$V(s) = \frac{m^2\omega_m^4}{64E_b}s^4 - \frac{m\omega_m^2}{4}s^2 \tag{4.1}$$

where $m = 1.0078$ amu is the mass of Hydrogen, ω_m is the frequency in the minimum potential energy and E_b is the depth of both wells (i.e. the barrier height). The values of each term are summed up in Tab. 4.1.

4.1.1 Resonance

The DW problem, in the absence of coupling with the bath, gives rise to the so called *Rabi oscillations*, characteristic of a complete and coherent transfer of population from one well to the other, whose period is determined by the *tunneling time*, as explained below. The DW potential can be studied as the overlap of two harmonic oscillators centered in its minima. Thus, we can obtain the eigenstates of the DW potential as the result of the harmonic eigenstate interaction. This leads to the

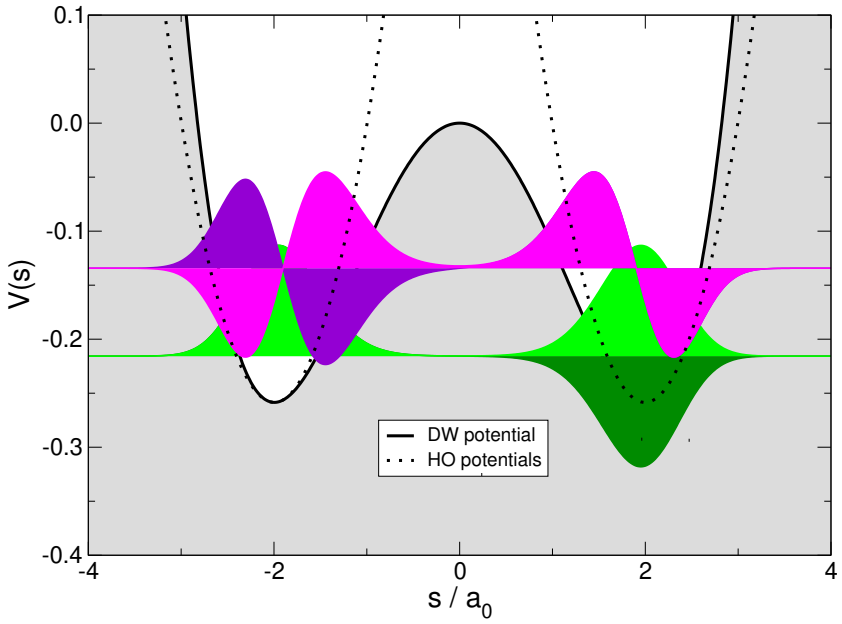

Figure 4.1: DW1 model potential and its first four eigenstates.

formation of a pair of DW eigenstates for each HO eigenstate couple, that differ by an energy ΔE_{ts} called *tunneling splitting*.

We can build the matrix of the DW Hamiltonian starting from the orthonormal basis functions of the two separated HOs, $|\chi_A\rangle$ and $|\chi_B\rangle$. Considering the Ground State (GS) we obtain

$$\mathbb{H} = \begin{bmatrix} \langle\chi_A|\mathcal{H}|\chi_A\rangle & \langle\chi_A|\mathcal{H}|\chi_B\rangle \\ \langle\chi_B|\mathcal{H}|\chi_A\rangle & \langle\chi_B|\mathcal{H}|\chi_B\rangle \end{bmatrix} = \begin{bmatrix} -\Delta\epsilon/2 & \mathcal{V} \\ \mathcal{V}^* & \Delta\epsilon/2 \end{bmatrix} \tag{4.2}$$

where $\mathcal{V}$ is the coupling strength between the two states and $\Delta\epsilon$ their energy difference. Diagonalizing this matrix we obtain the eigenvalues $\epsilon_\pm$:

$$\epsilon_\pm = \pm\sqrt{\frac{\Delta\epsilon^2}{4} + |\mathcal{V}|^2} = \pm\Omega \tag{4.3}$$

In the symmetric potential there is no energy difference between the starting states, i.e. $\Delta\epsilon$ is equal to zero, and this leads to the formation of resonant states. Thus, in this case the DW eigenstates simply result to be

$$\epsilon_\pm \equiv \pm|\mathcal{V}| \tag{4.4}$$

The eigenfunctions $\mathbb{C}^\pm$ can be calculated by the well known eigenvalue-eigenvector equation:

$$\mathbb{H}\mathbb{C}^\pm = \pm\Omega\mathbb{C}^\pm \tag{4.5}$$

Requiring the normalization condition, we obtain the two product states

$$|\psi_0\rangle = \frac{1}{\sqrt{2}}\left(|\chi_A\rangle + |\chi_B\rangle\right) \quad \text{and} \quad |\psi_1\rangle = \frac{1}{\sqrt{2}}\left(|\chi_A\rangle - |\chi_B\rangle\right) \tag{4.6}$$

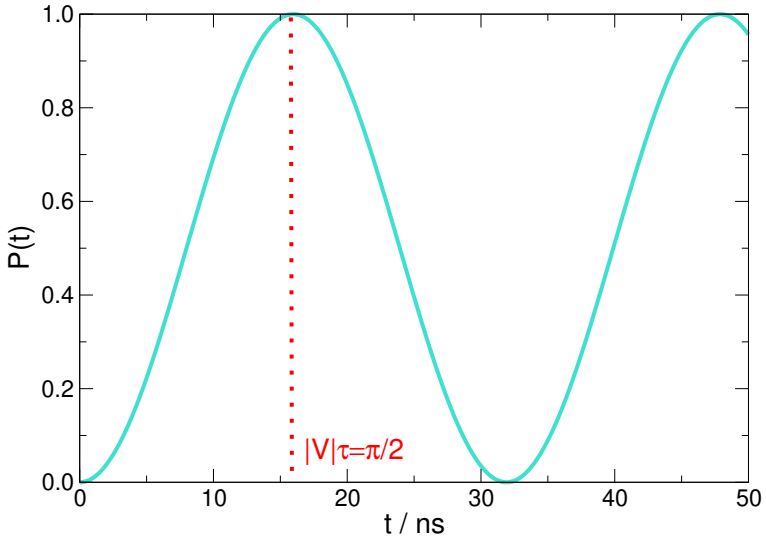

Figure 4.2: Transfer probability as a function of time.

In the eigenstate basis of the Hamiltonian the time evolution operator reads as

$$\mathbb{U}_t = \sum_i e^{-\frac{i}{\hbar}\epsilon_i t}\mathbb{P}_i \tag{4.7}$$

where $\mathbb{P}_i$ is the eigenprojector on the relevant i-th eigenstate, defined as $\mathbb{P}_i = \mathbb{C}_i\mathbb{C}_i^\dagger$. Therefore, the time evolution operator for the symmetric potential is

$$\mathbb{U}_t = \frac{1}{|\mathcal{V}|}\begin{bmatrix} |\mathcal{V}|\cos(|\mathcal{V}|t) & -i\mathcal{V}\sin(|\mathcal{V}|t) \\ -\mathcal{V}^*\sin(|\mathcal{V}|t) & |\mathcal{V}|\cos(|\mathcal{V}|t) \end{bmatrix} \tag{4.8}$$

If we want to study the transition from one well to the other we have to initialize the system in the first one, and then evolve it. The time-dependent probability reads as

$$P_{B\leftarrow A}(t) = |\langle\chi_B|U_t|\chi_A\rangle|^2 = \sin^2(|\mathcal{V}|t) \tag{4.9}$$

The sinusoidal function obtained means that the probability is affected by continuous oscillations, called Rabi oscillations (Fig. 4.2), and never reaches a plateau, as instead predicted by the kinetic theory. The maximum probability is equal to 1, i.e. there is complete transmission, and it is reached after the tunneling time τ

$$\tau = \frac{\pi}{2|\mathcal{V}|} \tag{4.10}$$

Since the Hamiltonian eigenvalues are $\epsilon_\pm = \pm\hbar\Omega$, their difference is $\Delta E_{ts} = 2\hbar\Omega$, and remembering that for the symmetric problem $\Omega = |\mathcal{V}|$, the tunneling time corresponds to

$$\tau = \frac{\hbar\pi}{\Delta E_{ts}} \tag{4.11}$$

For the system we studied $\Delta E_{ts} \simeq 1.3 \cdot 10^{-7}$ eV, so the tunneling time turns out to be $\tau \simeq 16\ ns$.

4.1.2 F_β eigenstates

From the Boltzmannized-Flux operator (F_β) diagonalization we obtain its eigenstates for different temperatures, whose shape is shown in Fig. 4.3. At $T = 0$ K the F_β eigenfunctions are symmetric and their spikes are centered in each well, while increasing the temperature they get close to each other until coalescence. Tab. 4.2 shows the energies of the most relevant eigenstates for each temperature considered (scaled by the GS zero point energy of -0.21564 eV). At higher temperatures the number of relevant states increases and they are characterized by greater energies.

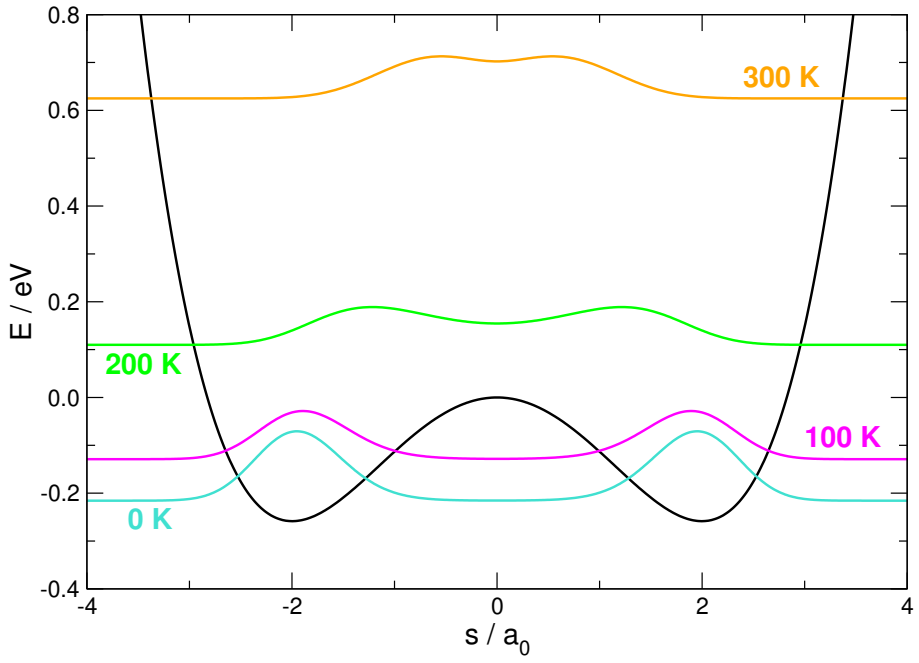

Figure 4.3: Boltzmannized-Flux operator eigenvectors for different temperatures.

Table 4.2: Energies of the relevant Boltzmannized-Flux operator eigenstates.

i	(T = 0 K)	T = 100 K	T = 200 K	T = 300 K
0	**0.0000E-00**	**8.6705E-02**	**3.2559E-01**	**8.4058E-01**
1	**0.0000E-00**	**8.6705E-02**	**3.2559E-01**	**8.4058E-01**
2	8.1322E-02	8.9459E-02	3.5208E-01	8.6634E-01
3	8.1341E-02	8.9459E-02	3.5208E-01	8.6635E-01
4	1.5391E-01	9.6125E-02	3.5740E-01	9.0656E-01
5	1.5482E-01	9.6125E-02	3.5740E-01	9.0682E-01
6	2.0837E-01	-	3.9464E-01	1.2903E-00
7	2.2109E-01	-	3.9464E-01	1.2821E-00
8	2.5714E-01	-	-	1.4138E-00
9	2.9006E-01	-	-	1.4109E-00

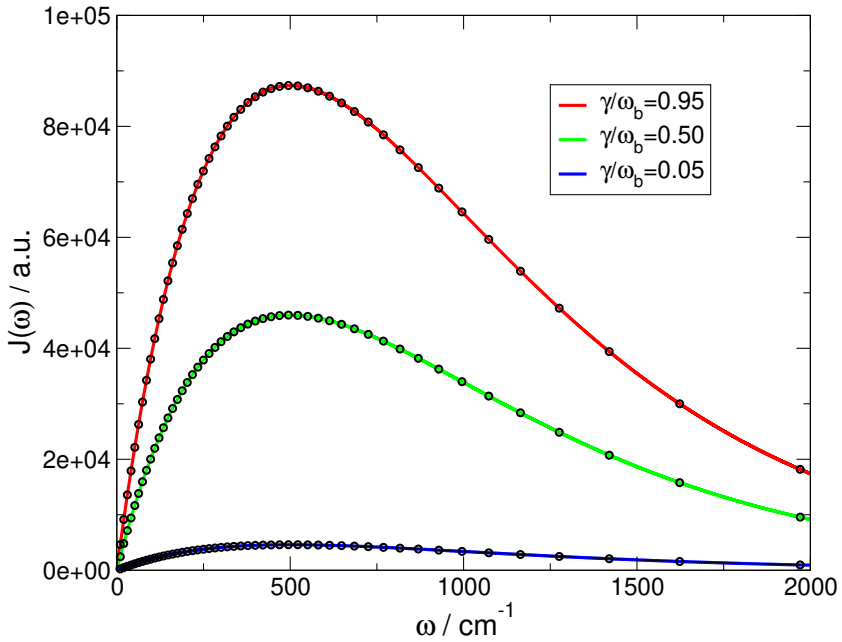

Figure 4.4: Spectral density for different friction values; the black circles represent the spectral density for the discrete frequencies of the bath.

4.2 Bath construction

The bath is built in order to describe a quasi-Markovian dynamics, directly comparable with the QUAPI calculation of Topaler and Makri [50] and the Craig et al. [44] ML-MCTDH results.

4.2.1 Quasi-Ohmic spectral density

We employ a quasi-Ohmic representation of the bath, described by a continuous spectral density function $J_O(\omega)$ (Fig. 4.4), which is linear with an exponential frequency cutoff:

$$J_O(\omega) = \gamma\omega e^{-\omega/\omega_c} \tag{4.12}$$

where γ corresponds to the system-bath coupling strength and the characteristic frequency ω_c is the frequency of maximum spectral density (see Tab. 4.1). For $\omega_c \to \infty$ the bath is strictly Ohmic, i.e. the dynamics of the system coordinate are described by the ordinary Langevin equation for the Brownian motion [51], and γ is the classically measurable friction. For finite values of ω_c, instead, the friction is non-local, and memory effects are introduced in the GLE.

The continuous spectral density can be discretized considering a set of N bath modes, each of them characterized by its proper frequency and coupling term. For an Ohmic bath the k-th frequency ω_k and the coupling parameter c_k are given by [43]

$$\omega_k = -\omega_c \ln\left(\frac{k}{N+1}\right) \tag{4.13}$$

$$c_k = \sqrt{\frac{2}{\pi}\frac{\gamma\omega_c}{N+1}}\omega_k \tag{4.14}$$

and the discretized spectral density results

$$J_O(\omega) = \gamma \sum_{k=1}^{N} \omega_k e^{-\omega_k/\omega_c} \ \delta(\omega - \omega_k) \tag{4.15}$$

Previous works in the literature considered a range of 60-150 HOs [44], but during our preliminary tests we found 50 HOs to be sufficient for a correct description of the kinetics.

4.2.2 Monte Carlo sampling

For each k-th HO we now have to choose the initial occupation of the energy levels. To this end we exploit the Monte Carlo sampling, which gives us a set of initial bath wave-functions with an energy Boltzmann distribution for each temperature of interest (see Section 3.2).

Convergence tests show that $\sim$ 200-300 Monte Carlo realizations are enough for an adequate convergence of the results, and Figs. 4.5 and 4.6 show the rapid convergence of the Monte Carlo sampling. Fig. 4.5 shows that at low temperature the correlation function is not affected by the number of sampling N_{MC} in a range of 50-800 (Fig. 4.5), while in Fig. 4.6 is plotted the kinetic constant relative error $\Delta k/k$ at high temperature, computed as

$$\frac{\Delta k}{k} = \frac{k - \bar{k}}{\bar{k}} \tag{4.16}$$

where $\bar{k}$ is the rate constant obtained after 1000 Monte Carlo realizations, considered as reference.

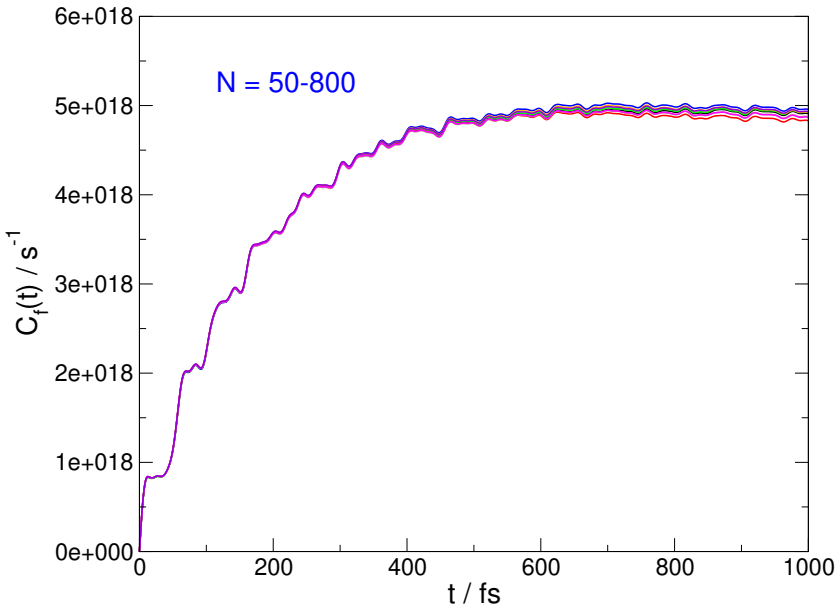

Figure 4.5: Correlation function $C_{fs}(t)$ obtained at $T = 100$ K for a number of Monte Carlo sampling N_{MC} variable in the range of 50-800.

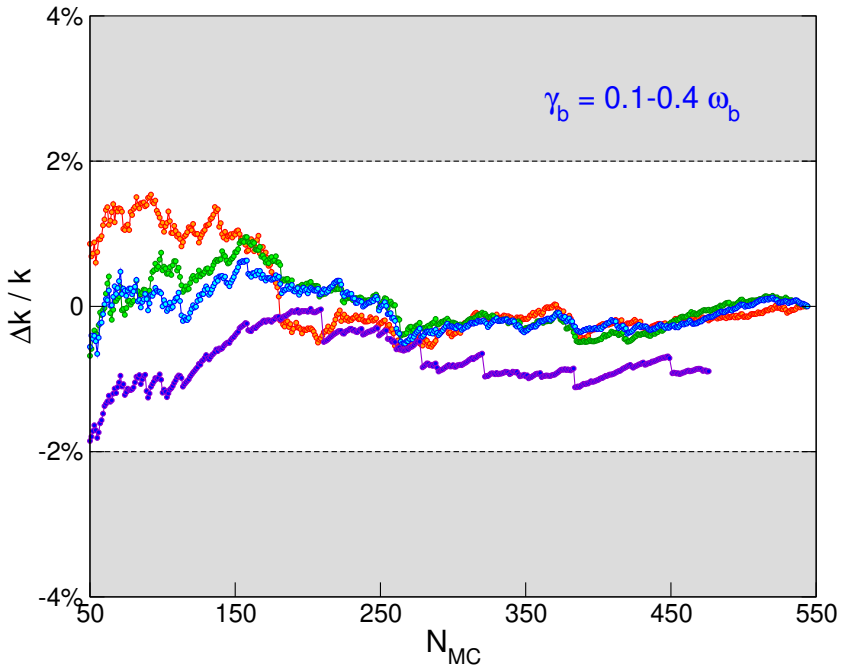

Figure 4.6: Estimated relative error of the rate constant as a function of the realization number, obtained at $T = 300$ K for different friction values in the range of 0.1-0.4 ω_b.

4.2.3 Multilayer test

The bath construction is the most delicate and time-consuming phase, because the results are significantly affected by its structure. A study of the branch connections and the number of SPFs that describe each of them is fundamental to build the most efficient multilayer tree.

In order to test the accuracy of the structures considered, we compare the results with previous works in the literature (as mentioned at the beginning of Section 4.2) and for high temperature ($T = 300$ K) we calculate an analytic approximation. We compute the transmission coefficient exploiting the Grote-Hynes' extension of the Kramers' theory [52], applicable in moderate and strong friction regime, i.e. valid for $\gamma/\omega_b > (\beta E_b)^{-1}$, with the Wolynes correction [50][53][54]. The Kramers-Grote-Hynes-Wolynes transmission coefficient reads as

$$\kappa_{\mathrm{KGHW}} = \kappa_{\mathrm{KGH}}\ \Xi = \frac{\lambda_0}{\omega_b}\ \Xi \tag{4.17}$$

where κ_{KGH} is the Kramers-Grote-Hynes transmission coefficient, Ξ is the Wolynes factor

$$\Xi = \prod_j^{+\infty} \frac{\omega_m^2 + j^2\nu^2 + j\nu\hat{\Gamma}(j\nu)}{-\omega_b^2 + j^2\nu^2 + j\nu\hat{\Gamma}(j\nu)} \tag{4.18}$$

with $\nu = 2\pi(\hbar\beta)^{-1}$, and λ_0 is the frequency of the unstable normal mode at the transition state computed by the Grote-Hynes equation:

$$\lambda_0 = \frac{\omega_b^2}{\lambda_0 + \hat{\Gamma}(\lambda_0)} \tag{4.19}$$

$\hat{\Gamma}(\lambda_0)$ and $\hat{\Gamma}(j\nu)$ are Laplace transforms of the memory kernel $\Gamma(t)$, respectively

$$\hat{\Gamma}(\lambda_0) = \int_0^{+\infty} dt\ \Gamma(t) e^{-\lambda_0 t} \quad \text{and} \quad \hat{\Gamma}(j\nu) = \int_0^{+\infty} dt\ \Gamma(t) e^{-j\nu t} \tag{4.20}$$

Fig. 4.7 shows some promising tree structures we tested, which provide a good reproduction of Craig et al. results [44], and we compute the average error on the transmission coefficient κ for each ML as

$$\langle \mathrm{ERR} \rangle = \left\langle \frac{\kappa - \kappa_{\mathrm{KGHW}}}{\kappa_{\mathrm{KGHW}}} \right\rangle \tag{4.21}$$

The first multilayer chosen, ML-Th, gives an error of 7% for the kinetic constants. It is characterized by an asymmetric structure, presents the two lowest energy oscillator paired, and the system coordinate is combined with its quasi resonant mode. Increasing the SPFs of each branch, we firstly improved the result reaching an error of 5%, but for a really high computational cost. Keeping on increasing the SPFs the error explodes, probably because of the sum of several computational approximations. We tried to isolate the lowest energy oscillator in a single branch and give a more symmetric structure to the tree (ML-c), but it provides the same error. Then, we built ML-a and ML-d, two trees with the system coordinate isolated in a single branch. Both of these trees present an isolated mode in the first branch of the deepest layer, but ML-a is characterized by higher symmetry. The error on the kinetic constant is 5%, and the increase of SPFs does not affect the results.

In Fig. 4.8 the kinetic coefficients are represented as a function of friction, computed for each ML structures. We notice that the ones obtained with ML-a and ML-d are really close to the Craig et al. results. In particular, for high value friction we improved their results. The average CPU times needed for each dynamics are summarized in Fig. 4.9, and the most efficient structure results to be ML-a, which provides the best compromise between result accuracy and computational cost.

4.3 Validation

In order to validate the methodology, we need to perform preliminary dynamics to be compared with Craig et al. results [44].

4.3.1 Grids

The hydrogen atom, i.e. the system, is represented on a DVR grid made up of 512 points, between -4 and +4 a_0, using the *Fast Fourier Transform* (FFT) algorithm. For the bath modes we used the HO grid with a variable point number, higher for modes with low frequency and lower for high frequency modes. Using a grid with n DVR points we can represent up to n-1 excited states. For this reason, while the system grid is kept fixed, the bath mode grid needs to be checked after the Monte Carlo sampling: if the latter generates an initial bath configuration with one or more occupied levels higher than n-1, the grid is expanded. In Tab. 4.3 we report the basic grid scheme for the system and each bath mode.

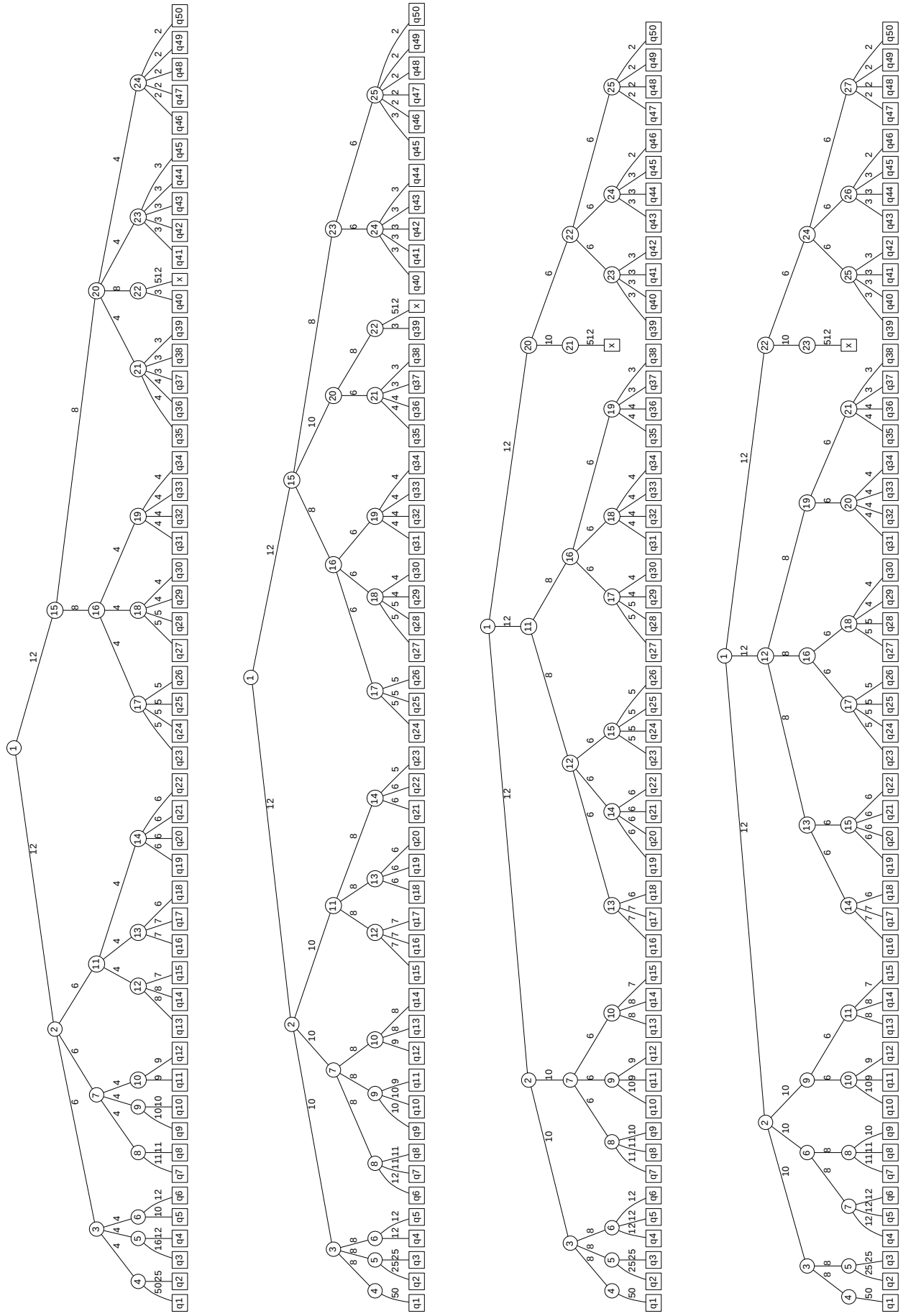

Figure 4.7: Tree structures. From the left: ML-Th, ML-c, ML-a and ML-d.

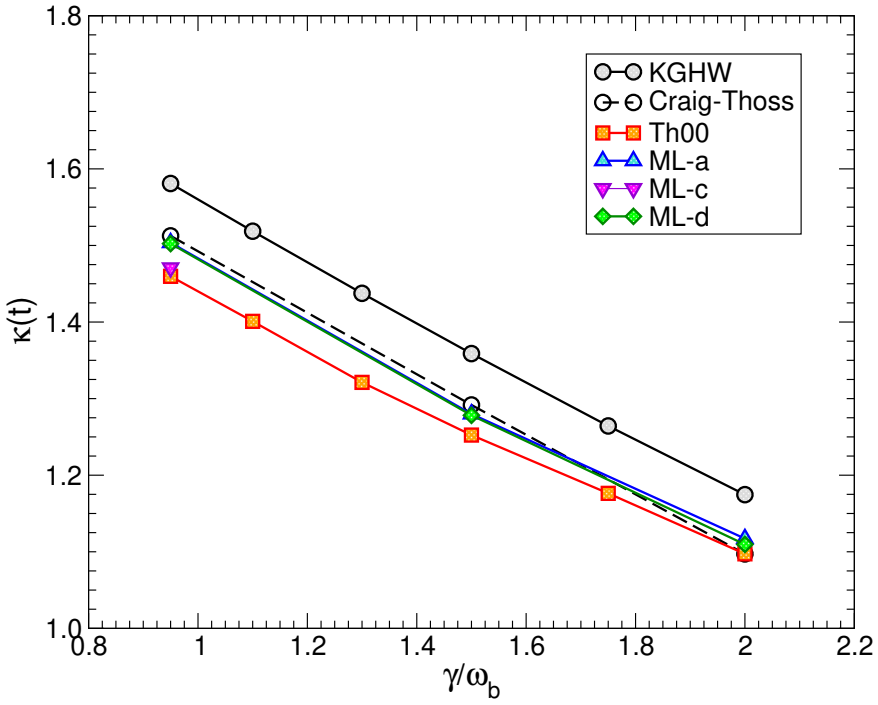

Figure 4.8: Kinetic coefficient as a function of γ/ω_b, computed for each ML structures.

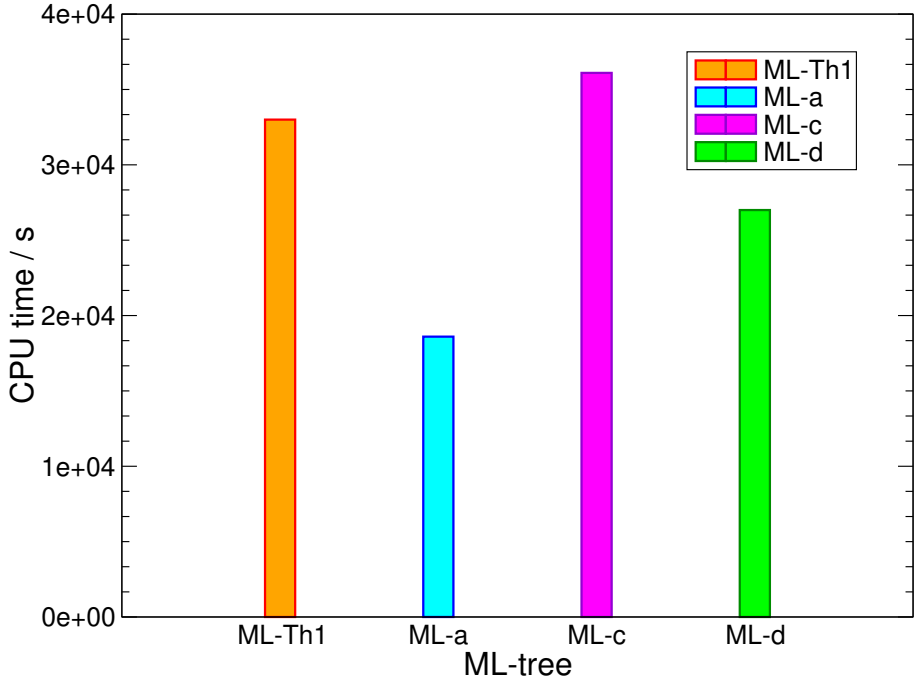

Figure 4.9: CPU time for each dynamics with each ML.

Table 4.3: Grid parameter for each mode.

mode	grid	DVR	mode	grid	DVR
x	FFT	512			
q1	HO	50	q26	HO	5
q2	HO	25	q27	HO	5
q3	HO	16	q28	HO	5
q4	HO	12	q29	HO	4
q5	HO	10	q30	HO	4
q6	HO	12	q31	HO	4
q7	HO	11	q32	HO	4
q8	HO	11	q33	HO	4
q9	HO	10	q34	HO	4
q10	HO	10	q35	HO	4
q11	HO	9	q36	HO	4
q12	HO	9	q37	HO	3
q13	HO	8	q38	HO	3
q14	HO	8	q39	HO	3
q15	HO	7	q40	HO	3
q16	HO	7	q41	HO	3
q17	HO	7	q42	HO	3
q18	HO	6	q43	HO	3
q19	HO	6	q44	HO	3
q20	HO	6	q45	HO	3
q21	HO	6	q46	HO	2
q22	HO	6	q47	HO	2
q23	HO	5	q48	HO	2
q24	HO	5	q49	HO	2
q25	HO	5	q50	HO	2

4.3.2 Results

We computed kinetic constants and transmission coefficients for a wide range of temperature and friction, and we succeeded in reproducing Craig et al. results [44], in each regime they considered. As shown in Figs. 4.10 and 4.11, the transmission coefficient trends are very different from each other. For strong coupling a clean plateau is easily reached, while for weak friction $\kappa(t)$ is affected by oscillations. This behavior depends on the dissipation speed of the energy from the system into the bath: when the coupling is strong the excess energy dissipation is fast, while it is really slow for small value of γ/ω_b. In the last case the system typically recrosses the reaction barrier several times before reaching the equilibrium, and this leads to the necessity of a larger propagation time.

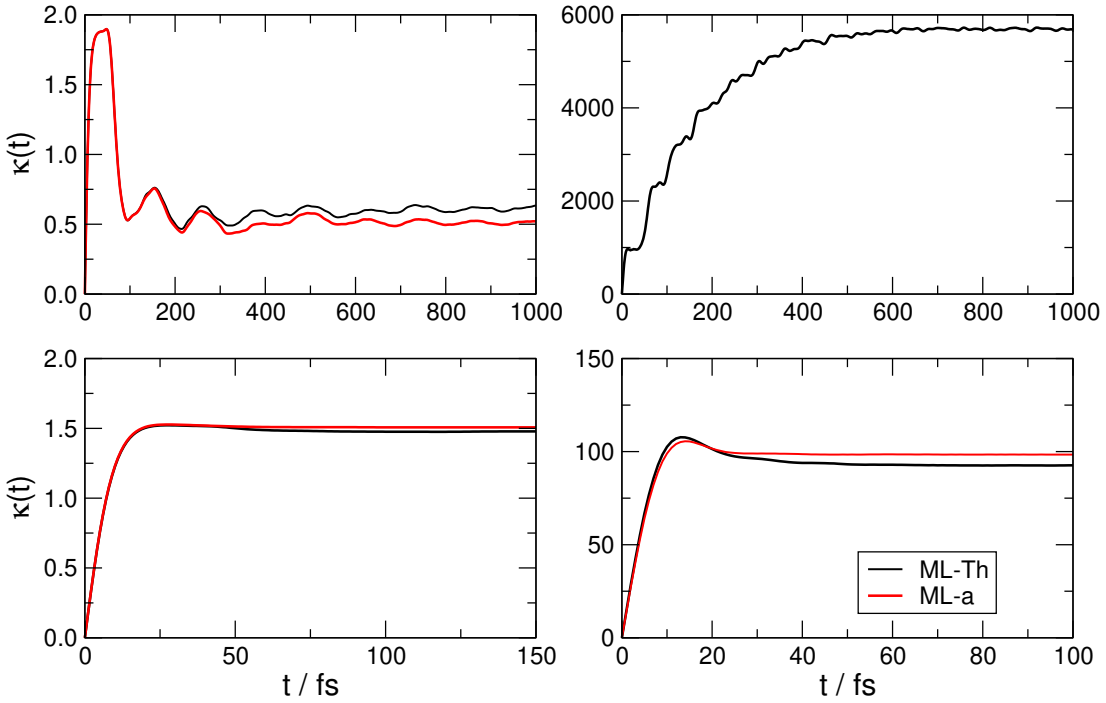

Figure 4.10: Our results for transmission coefficients as a function of time. Each graph represents a different temperature and friction regime: $T = 300$ K for left panels, $\gamma = 0.05\ \omega_b$ at the top and $\gamma = 0.95\ \omega_b$ at the bottom, $T = 100$ K for right graphs, $\gamma = 0.01\ \omega_b$ at the top and $\gamma = 0.95\ \omega_b$ at the bottom.

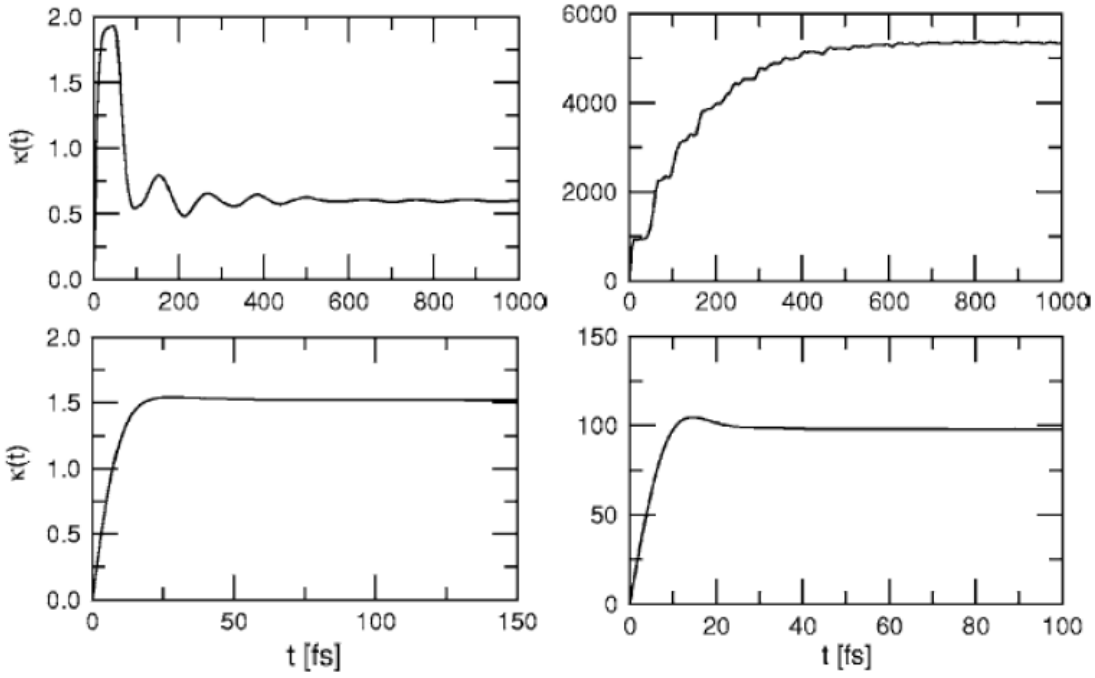

Figure 4.11: Craig et al. results [44] (same disposition of the previous figure).

Chapter 5

Quantum-classical crossover

For processes like the ones we model here, there exists a temperature at which tunneling and thermally activated barrier crossing are roughly equally relevant, the so called *crossover temperature* [18][19][20][21]. This characteristic temperature as a function of friction is plotted in Fig. 5.1, expressed as in Eq. 1.1:

$$T_c = \frac{\hbar \lambda_0}{2\pi k_B}$$

where λ_0 is the unstable frequency at the top of the barrier given by Eq. 4.19:

$$\lambda_0 = \frac{\omega_b^2}{\lambda_0 + \hat{\Gamma}(\lambda_0)}$$

which decreases as a function of friction.

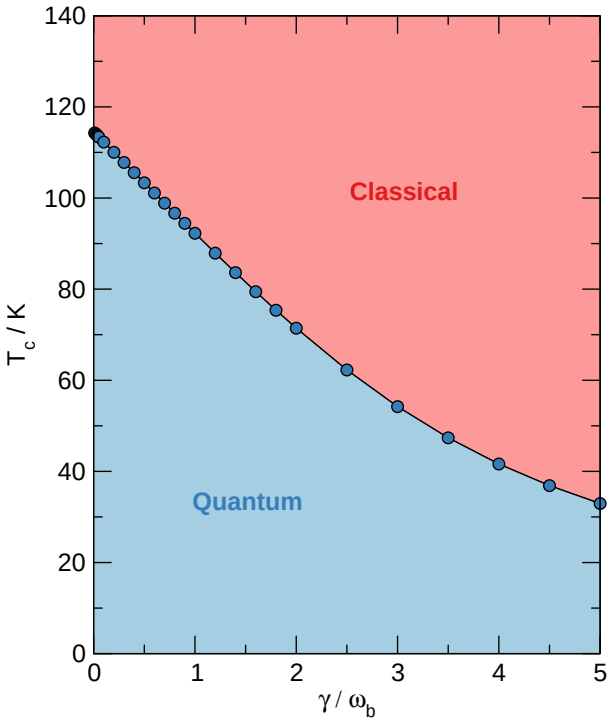

Figure 5.1: Crossover temperature as a function of friction.

In this chapter we introduce the theoretical derivation of Eq. 1.1 [55] and explain in details the results obtained from our simulations, focusing on the quantum-classical crossover marked by T_c.

5.1 Crossover temperature

The T_c expression in Eq. 1.1 is valid for a parabolic barrier [55], for which the transition probability in the quasi-classical form reads as

$$W(E) = \frac{1}{1 + \exp\left(\frac{2\pi(E_b - E)}{\hbar\lambda_0}\right)} \tag{5.1}$$

where E is the reactant energy [56][57]. The thermally averaged probability P is given by

$$P = \int_0^{+\infty} W(E)\ e^{-\frac{E}{k_B T}}\ \frac{dE}{k_B T} \tag{5.2}$$

and in the classical limit reads as

$$P^{cl} = e^{-\frac{E_b}{k_B T}} \tag{5.3}$$

since $W(E) = 0$ if $E < E_b$ and $W(E) = 1$ for $E > E_b$. The transmission coefficient can be computed as the ratio between the total and the classical probabilities:

$$\kappa = \frac{P}{P^{cl}} = \int_{-E_b}^{+\infty} \frac{\exp\left(-\frac{\epsilon}{k_B T}\right)}{1 + \exp\left(-\frac{2\pi\epsilon}{\hbar\lambda_0}\right)} \frac{d\epsilon}{k_B T} \tag{5.4}$$

where $\epsilon = E - E_b$. This integral can be decomposed in two parts, $\kappa' = P'/P^{cl}$ and $\kappa'' = P''/P^{cl}$, computed respectively in the intervals $[-E_b, 0]$ and $[0, +\infty)$. The integral in Eq. 5.4 can be easily solved if the exponential arguments are the same, i.e. if

$$\frac{2\pi}{\hbar\lambda_0} = \frac{1}{k_B T} \tag{5.5}$$

In that case we obtain

$$\kappa' = \arctan\left[\exp\left(\frac{E_b}{k_B T}\right)\right] - \frac{\pi}{4} \quad \text{and} \quad \kappa'' = \frac{\pi}{4} \tag{5.6}$$

The crossover temperature can be calculated from the condition

$$\frac{P'}{P''} = \frac{\kappa}{\kappa''} = 1 \tag{5.7}$$

which is guaranteed for $E_b \gg k_B T$ [55][58][59], in fact in this limit

$$\arctan\left[\exp\left(\frac{E_b}{k_B T}\right)\right] \to \frac{\pi}{2} \quad \text{and} \quad \kappa' \to \frac{\pi}{4} = \kappa'' \tag{5.8}$$

Thus, for a parabolic barrier characterized by $E_b \gg k_B T$, the condition in Eq. 5.7 is met if the temperature satisfies Eq. 5.5, i.e. if T is given by Eq. 1.1.

5.2 Results

We scanned the temperature space from $T = 100$ K to $T = 300$ K considering a range of friction between $\gamma = 0.01\ \omega_b$ and $\gamma = 5.00\ \omega_b$, in order to study how the kinetic constant and the transmission coefficient behave passing from the quantum to the classical regime. All of the results presented in this section are obtained with ML-a (Fig. 4.7).

In Tab. 5.2 are summarized all the κ values computed by Eq. 3.2. Their trend as a function of γ/ω_b plotted in Fig. 5.2 shows a temperature-dependent behavior. In order to study in details this behaviour, we focus on the two extreme temperatures and an intermediate one ($T = 200$ K), whose trends are shown in Fig. 5.3, represented on different scales (linear and logarithmic for both axes). At very low temperatures the reaction is dominated by quantum effects and the transmission coefficients are large, especially for low friction. The monotonic decrease characteristic of this regime is due to the coherence decrease combined with the energy dissipation increase. At high temperatures the transmission coefficient rises to a maximum and then decreases, exhibiting the turnover behaviour predicted by the Kramers' theory [22][23], assuming that the barrier height is much greater than the thermal energy of the system: $E_b \gg k_B T$ (for $T = 300$ K, $E_b = 10\ k_B T$). Our results for these regimes are in agreement with the literature and confirm the theoretical predictions explained in Section 1.3.1. For intermediate temperatures, instead, the transmission coefficient trend is affected by an anomalous inflection for low friction values, never observed before. This trend is a mixture of the ones described for low and high temperature, and it should be the quantum-classical crossover signal. For these conditions no information is present in the literature, so a more detailed investigation of the low coupling regime is necessary .

In Fig. 5.4 is shown $\kappa(t)$ for very weak friction values ($\gamma \leq 0.05\ \omega_b$), obtained for different temperatures. At a fixed temperature each curve reaches the same plateau at about ~ 50 fs, which corresponds to the *coherence time* of the bath, i.e. the time the system needs to "feel" the environment. All of the transmission coefficients oscillate with time before stabilizing at the *plateau*, because of the slow energy dissipation occurring for low friction, but these oscillations become much more pronounced and irregular for intermediate temperature. Thus, for this regime longer propagation times are needed for accurate results since this effect makes difficult determining the transmission coefficient, not reaching a well defined plateau easily. This convergence problem is probably due to the competition between different effects in this sensitive transitory regime.

Table 5.1: κ for each temperature-friction combination.

γ/ω_b	*T=100 K*	*T=125 K*	*T=150 K*	*T=175 K*	*T=200 K*	*T=300 K*
0.01	1.84787E+05	1.48282E+02	2.17702E+01	6.00619E+00	2.34257E+00	3.32700E-01
0.02	3.04962E+03	8.45169E+01	1.38289E+01	3.87677E+00	1.53335E+00	2.98290E-01
0.03	2.11045E+03	6.36165E+01	1.07480E+01	3.35292E+00	1.42957E+00	3.49281E-01
0.04	1.62092E+03	5.32100E+01	9.77694E+00	3.25452E+00	1.57268E+00	4.41504E-01
0.05	1.33287E+03	4.72093E+01	9.44846E+00	3.38102E+00	1.74961E+00	5.19763E-01
0.10	7.80130E+02	3.73032E+01	9.14234E+00	4.21848E+00	2.42602E+00	8.28176E-01
0.20	4.98156E+02	3.52108E+01	1.05398E+01	5.23685E+00	3.27548E+00	1.29140E+00
0.40	2.93980E+02	3.03277E+01	1.03720E+01	5.51624E+00	3.65851E+00	1.61897E+00
0.60	1.83327E+02	2.54718E+01	9.42046E+00	5.18597E+00	3.47920E+00	1.63923E+00
0.80	1.25868E+02	2.16441E+01	8.59720E+00	4.80795E+00	3.21705E+00	1.56481E+00
0.95	9.88220E+01	1.93215E+01	7.97009E+00	4.53637E+00	3.00007E+00	1.50699E+00
1.10	7.93020E+01	1.73426E+01	7.41860E+00	4.24829E+00	2.91333E+00	1.44896E+00
1.30	5.99437E+01	1.50004E+01	6.72019E+00	3.90827E+00	2.70200E+00	1.37420E+00
1.50	4.70402E+01	1.30187E+01	6.06597E+00	3.62798E+00	2.49904E+00	1.29646E+00
1.75	3.74995E+01	1.11077E+01	5.38760E+00	3.26671E+00	2.29018E+00	1.21080E+00
2.00	3.20141E+01	9.67009E+00	4.81554E+00	2.95923E+00	2.09014E+00	1.12994E+00
5.00	3.99888E+00	2.67001E+00	1.61275E+00	1.09421E+00	7.97263E-01	5.38426E-01

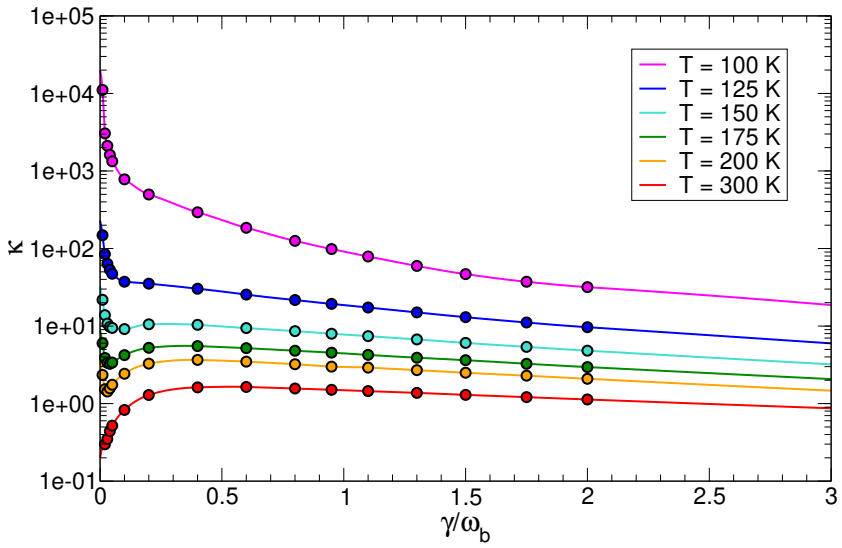

Figure 5.2: Transmission coefficient as a function of friction at different temperatures.

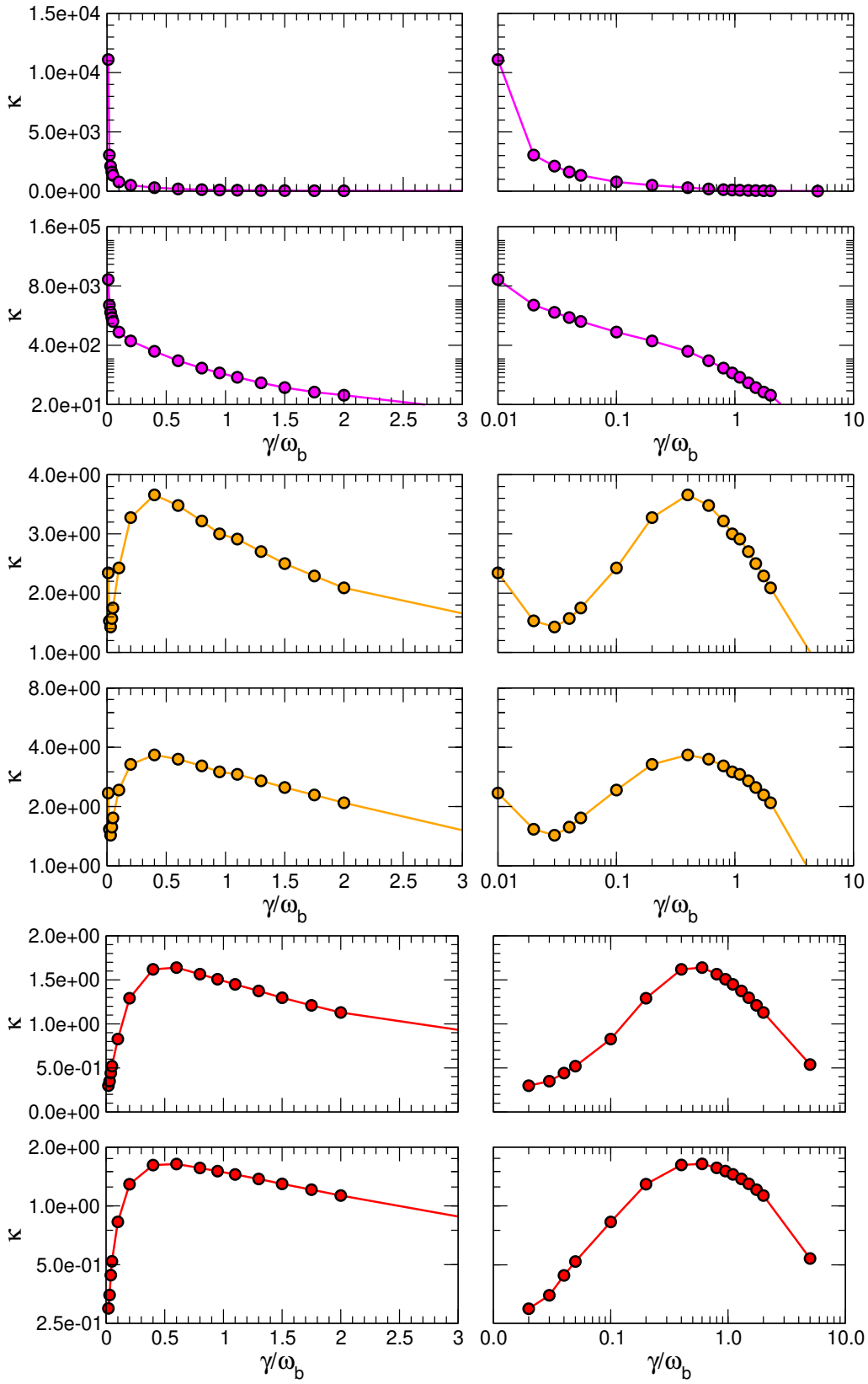

Figure 5.3: Transmission coefficient as a function of friction at $T = 100$ K (pink), $T = 200$ K (orange) and $T = 300$ K (red). For each colour block: both axes on a linear scale (top-left), vertical axis on a linear scale and horizontal axis on a logarithmic scale (top-right), vertical axis on a logarithmic scale and horizontal axis on a linear scale (bottom-right), both axes on a logarithmic scale (bottom-left).

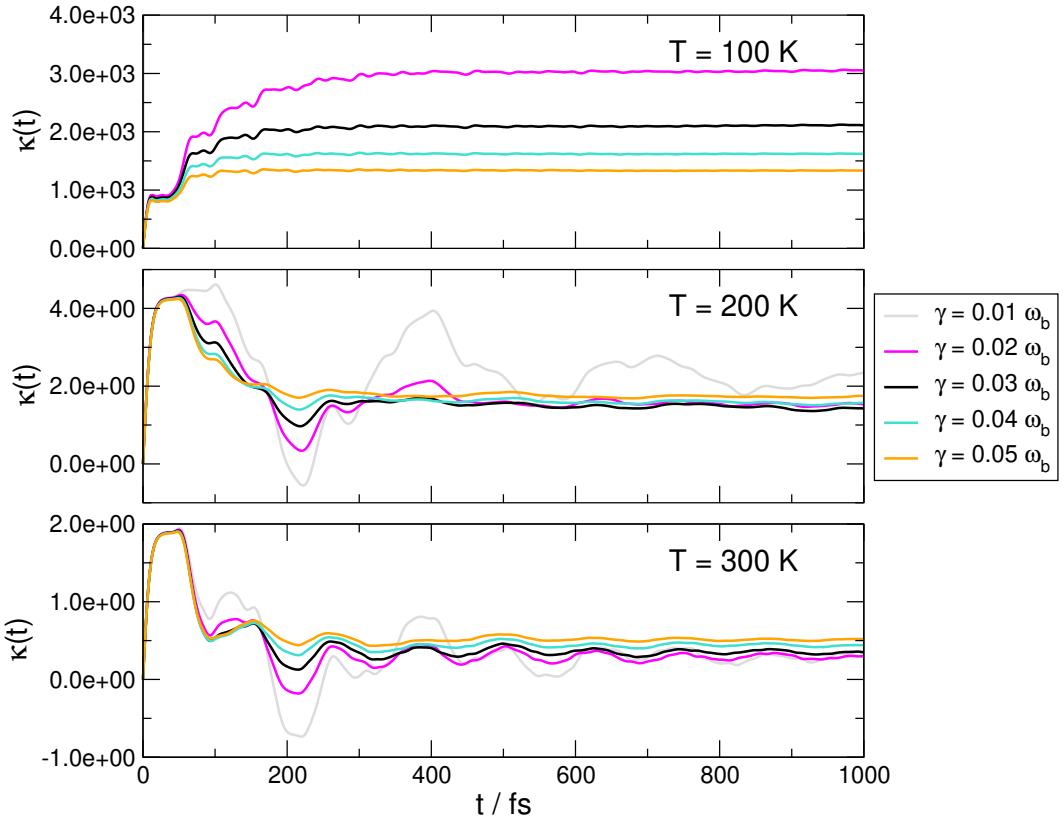

Figure 5.4: Transmission coefficient as a function of time at different friction values. Three temperature regimes are here represented: 100 K in the top panel, 200 K in the middle one and 300 K in the bottom plot.

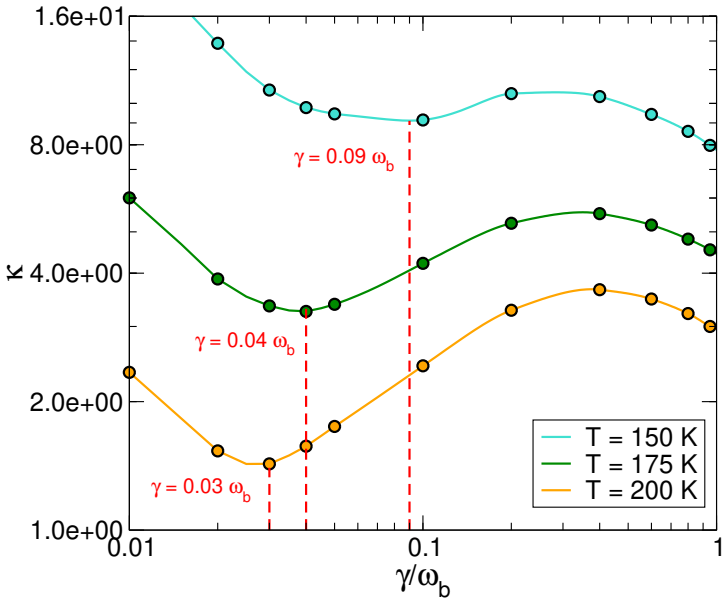

Figure 5.5: Transmission coefficient as a function of friction for intermediate temperatures and weak coupling.

5.2.1 Study of the minimum

In order to investigate the crossover region, we focus on the minimum κ for weak friction, and we assume it signals the crossover from the quantum to a classical behaviour. Fig. 5.5 shows how increasing the temperature the minimum moves to lower values of friction. In Fig. 5.1 T_c is always less than 114.3 K (the crossover temperature for γ tending to 0), but we find the trend inversion in a range of temperature between 150 and 200 K. As shown previously, T_c can be analytically computed knowing the frequency at the transition state, which depends on the coupling strength that lowers the effective imaginary frequency at the top of the barrier ($\omega_b \to \lambda_0$). We compute the effective frequency of the unstable mode for the friction values of minimum κ from Eq. 4.19, summarized in Tab. 5.2 along with their corresponding crossover temperatures.

As is evident from the table, the temperatures T investigated (first column of the table), which define the range of T values over which a transition is apparent, are markedly larger than the crossover temperatures for the given values of γ (last column of the table). Thus, in our system Eq. 1.1 is not a reliable estimate of the temperature at which the transition from classical to quantum behaviour occurs. In fact, the effective potential barrier is not strictly parabolic, as instead needed for Eq. 1.1 to hold, and the crossover temperature defined in this way becomes of limited help.

Table 5.2: Quantum-classical crossover points.

T / K	γ/ω_b	λ_0 / cm^{-1}	T_c / K
150	0.09	491	112.5
175	0.03	497	113.8
200	0.02	498	114.0

5.2.2 Arrhenius plot

The kinetic constant obtained by ML-MCTDH dynamics are reported in the Arrhenius plot shown in Fig. 5.6.

For high temperatures, the rate constant exhibits the typical trend predicted by Arrhenius theory, and we calculated the effective activation energies $\tilde{E}_a$ through the Arrhenius law

$$k(T) = A \ \exp\left(-\frac{\tilde{E}_a}{k_B T}\right) \tag{5.9}$$

where A is the Arrhenius coefficient. Linearizing Eq. 5.9 gives

$$\ln k = \ln A - \frac{\tilde{E}_a}{k_B}\frac{1}{T} \tag{5.10}$$

where $\tilde{E}_a$ is the slope multiplied by $-k_B$. Fig. 5.7 shows the regression lines (dashed lines) of $\ln k$ computed in the range of temperature between 300 and 150 K for the friction values considered in Fig. 5.6. In Tab. 5.3 are reported the effective activation energies obtained as described above. R1, R2 and R3 represent the range of temperature considered for the linear regressions, respectively 300-200 K, 300-175 K and 300-150 K. As shown in this table, the activation energies increase with friction, tending to the theoretical value $E_b = 2085$ cm^{-1}. The lowering of the activation energy is related to the zero-point effects associated with the presence of friction [60], showing the limit of TST theory in the friction regimes considered. It is known in the literature that TST theory properly describes the dynamics only for high values of friction, in the so called *spatial diffusion* regime, while for weak friction, the *energy diffusion* regime, is completely inadequate. Moreover, k is the classical rate computed with the quantum partition function of the reagents, so its dependence on T is not the classical $\hbar\omega_b/(k_B T)$ and it is affected by coupling effects. Thus, the classical linear limit is reached only if $k_B T \gg \omega_b$, which means that for our potential ($\omega_b = 500$ cm^{-1}) that corresponds to $T \simeq 720$ K.

At low temperature dissipation plays a very important role: for weak friction the rate is no more the one predicted by Arrhenius and it tends to the value determined by tunneling, while for stronger coupling k decreases smoothly. In the limit of infinitely weak friction the kinetic constant does not depend on temperature anymore and reaches a well-defined plateau. This friction dependence observed for the Arrhenius plot is in agreement with the semiclassical results [50][61].

Table 5.3: Activation energies for different friction values.

γ/ω_b	$\tilde{E}_a^{R1}$ / cm^{-1}	$\tilde{E}_a^{R2}$ / cm^{-1}	$\tilde{E}_a^{R3}$ / cm^{-1}
0.01	1268	1243	1214
0.10	1585	1612	1585
0.40	1742	1727	1699
0.95	1795	1767	1738
1.50	1808	1787	1784
5.00	1918	1883	1855

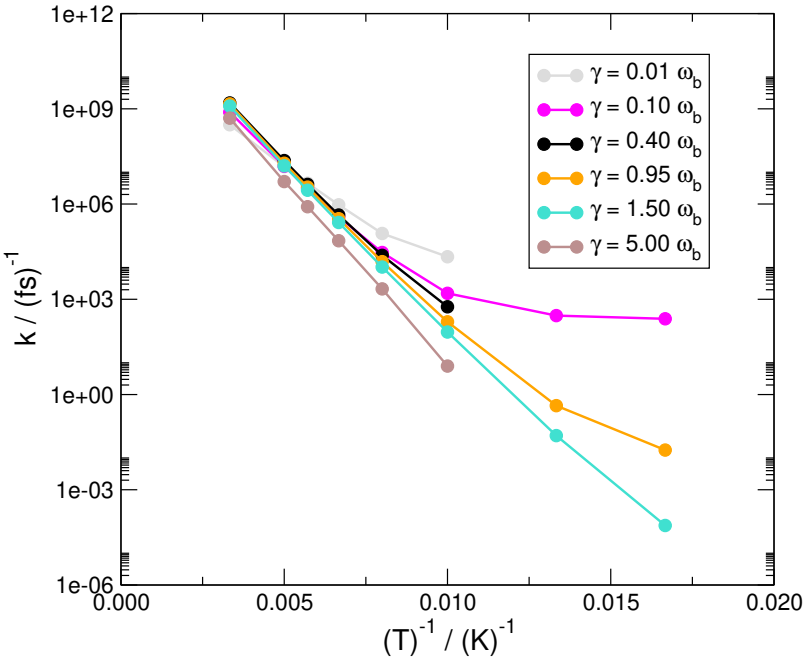

Figure 5.6: Arrhenius plot for different coupling strength values.

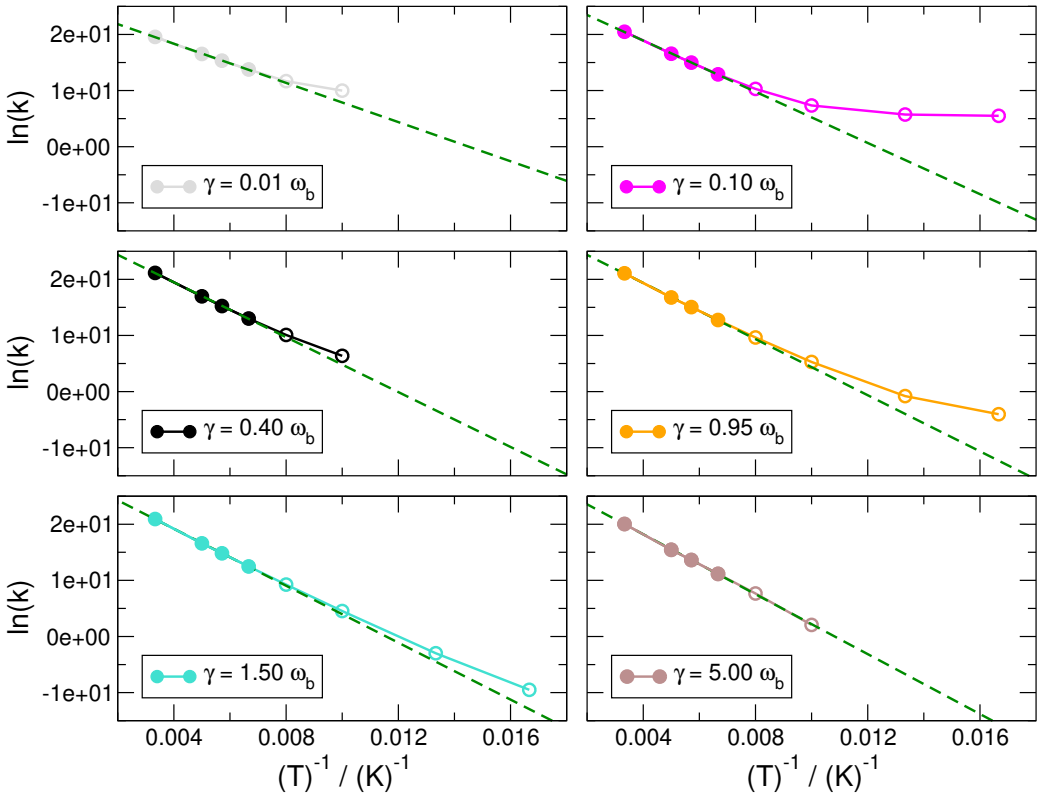

Figure 5.7: Arrhenius plot for different friction and linear regression (dashed lines) of the classical region (300-150 K).

Chapter 6

RPI benchmarks

The results of this work have been useful as a benchmark for the Ring-Polymer Instanton (RPI) approach [62], another possible way to implement the tunneling effect in the rate theory. We collaborated with Professor Jeremy Richardson and his student Michael Müller, who studied the DW system discussed so far, and in this chapter we show the comparison between their and our results.

6.1 Theoretical introduction

The semiclassical instanton rate theory is a quantum-mechanical generalization of TST, where the tunneling is described as the dynamics of the *instanton*, a periodic classical orbit of imaginary-time length $\beta\hbar$ which traverses the barrier region [63]. The instanton theory is the only one that uses and defines the optimal pathway for the tunneling process [64], the so called *instanton path* (Fig. 6.1), which can only be found below the crossover temperature[18]. In this approach the rate constant is computed as

$$k_{inst} = A_{inst}\ e^{-\frac{S}{\hbar}} \tag{6.1}$$

where A_{inst} is a measure of fluctuations around the instanton path and S is the Euclidean action along the instanton trajectory [64].

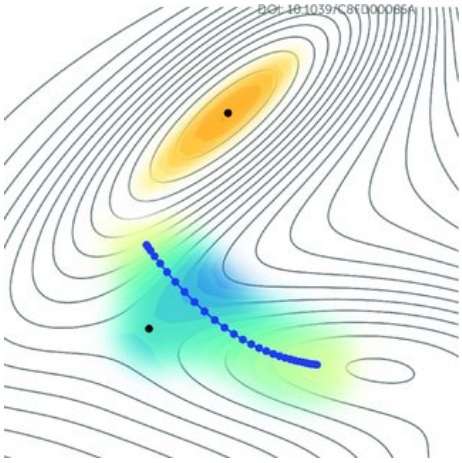

Figure 6.1: Representation of instanton path (blue line) [65].

The ratio between the instanton rate and TST defines the tunneling factor, analogously to the transmission coefficient.

The most common discretization scheme used for representing closed path integrals is the ring polymer, where the path is represented by N beads x_i. Each bead is an image of the f-dimensional system, characterized by the ring-polymer potential [62]:

$$U_N(x) = \sum_{i=1}^{N} \frac{mN^2}{2\beta^2\hbar^2}|x_i - x_{i-1}|^2 + \sum_{i=1}^{N} V(x_i) \tag{6.2}$$

In the RPI theory, the rate constant and the partition function can be obtained with a similar approach as that in Eyring TST, using following formulas. The partition function in this representation reads as [62]

$$Z_{inst} = -\left(\frac{2\pi\beta\hbar^2}{mN}\right)^{-\frac{Nf}{2}} \int e^{-\frac{\beta}{N}U_N(x)} dx \tag{6.3}$$

and the kinetic constant is given by

$$k_{inst}(T) = \frac{1}{2\pi\beta\hbar} \frac{Z_{inst}}{Z_r(T)} e^{-\frac{S}{\hbar}} \tag{6.4}$$

where $Z_r(T)$ is the reactant partition function, $Z_{inst}(T)$ is the instanton partition function and S is here the action of the ring-polymer pathway [62]:

$$S = \hbar\frac{\beta}{N}U_N(x) \tag{6.5}$$

The expression of k_{inst} in Eq. 6.4 could be considered as a finite N-dimensional version of TST, which tends to Eq. 3.1 in the limit of $N \to \infty$, where $S/\hbar$ is replaced by βE_a.

6.2 RPI-MCTDH comparison

The main goal of the Richardson and Müller work was to reproduce our MCTDH results and to test the boundaries of the RPI for this model system. The bottom limit for instanton calculation was found at $T = 50$ K, while the upper limit was considered at $T = 100$ K, but strongly depends on friction (see Chapter 5).

Since their approach is valid only below T_c, we had to extend the temperature region of study. The comparison is shown in Fig. 6.2, where the lines joining the points are only drawn to guide the eye. For a medium-strong coupling regime the qualitative trend of the RPI curves coincides with the MCTDH ones, but for low friction the RPI rate is not a good approximation.

Unfortunately, both the RPI and MCTDH data sets are not yet complete. Moreover, for the extremely low temperature regime, the rate constant calculations with MCTDH turn out to be really expensive, because of the increasingly long imaginary-time propagations required and, for the weak coupling regime, the extremely long propagation times needed to reach a plateau. Therefore, this study is still ongoing.

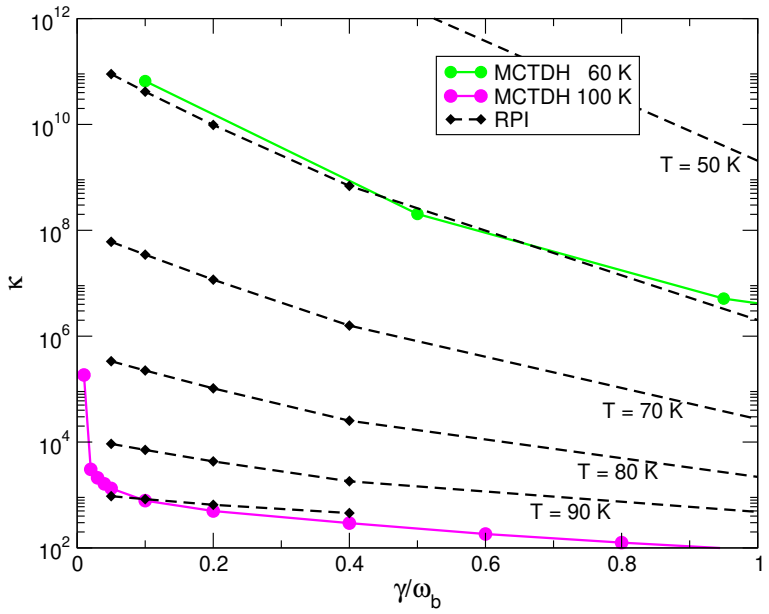

Figure 6.2: Transmission coefficient as a function of friction for different temperatures. RPI results with dotted lines.

Chapter 7

Effective mode representation

A smart way to reduce the computational effort consists in the effective mode discretization of the bath described in Section 2.3. As explained in that part, we obtain the parameters of the effective modes through the deconvolution of the spectral density, and we use these parameters to describe the bath DOFs back in the normal mode representation.

The spectral density considered in the following sections is characterized by a friction $\gamma = 0.95\,\omega_b$, for which we study how bath properties change with the number of modes considered. The dynamics are performed at $T = 100$ K and we describe the convergence of our results as a function of the bath dimension.

7.1 Bath properties

We employed up to 100 HOs, and in this section we show the characteristics of some example baths considered.

The deconvolution of the spectral density leads to the sequence $\{J_n(\omega)\}_{n\in N}$, whose convergence is easily reached, already for a bath composed by 10 HOs, as evident in Fig. 7.1.

In Fig. 7.2 are shown the coupling parameters of each k-th HO as a function of its frequency, between which there is no more the linear dependence described in Eq. 4.14. The bath frequency definition given by Eq. 4.13 leads to a non-homogeneous spacing, with a density that decreases as the frequency increases. In this new discretization we have the opposite trend: the frequency spacing reduces for higher values of ω_k. Moreover, for the same frequency, c_k assumes different values as a function of the bath dimension, decreasing when more modes are added.

The other important aspect to take into account is the memory kernel. If the bath is too small, the energy released into the environment comes back to the system, like if it was coupled with itself. This undesirable effect is avoidable using an appropriate number of modes for a certain propagation time. The memory kernel as a function of time is plotted in Fig. 7.3, and its stability increases with the bath dimension, approaching the plateau represented by the black dashed line. From its behavior we can mark the maximum time limit within which our dynamics have a physical sense.

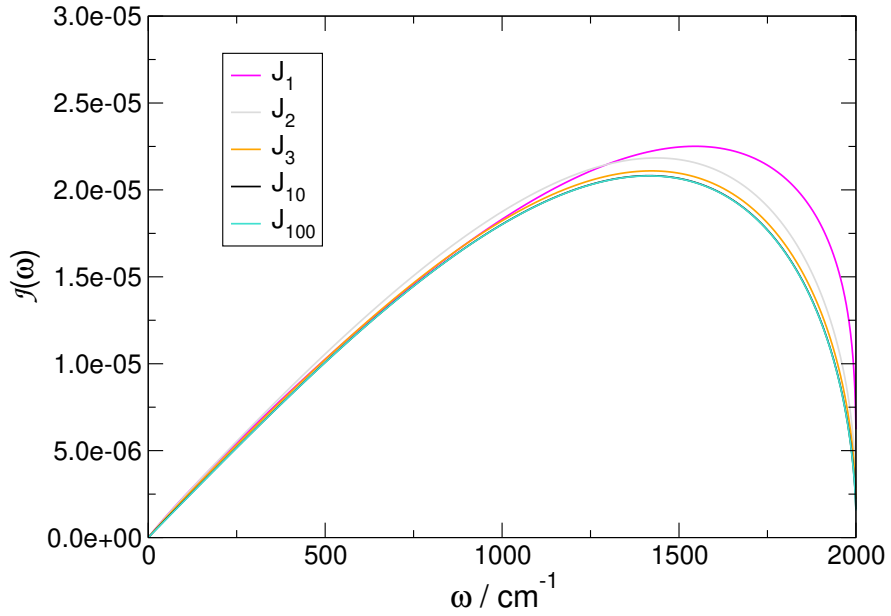

Figure 7.1: Convergence of the spectral density deconvolution.

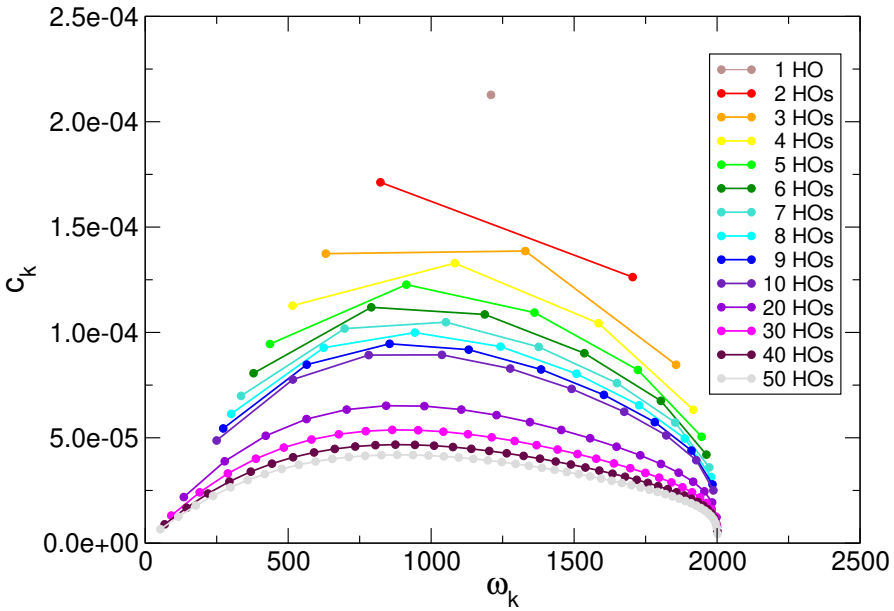

Figure 7.2: Coupling coefficient as a function of frequency for different bath dimensions.

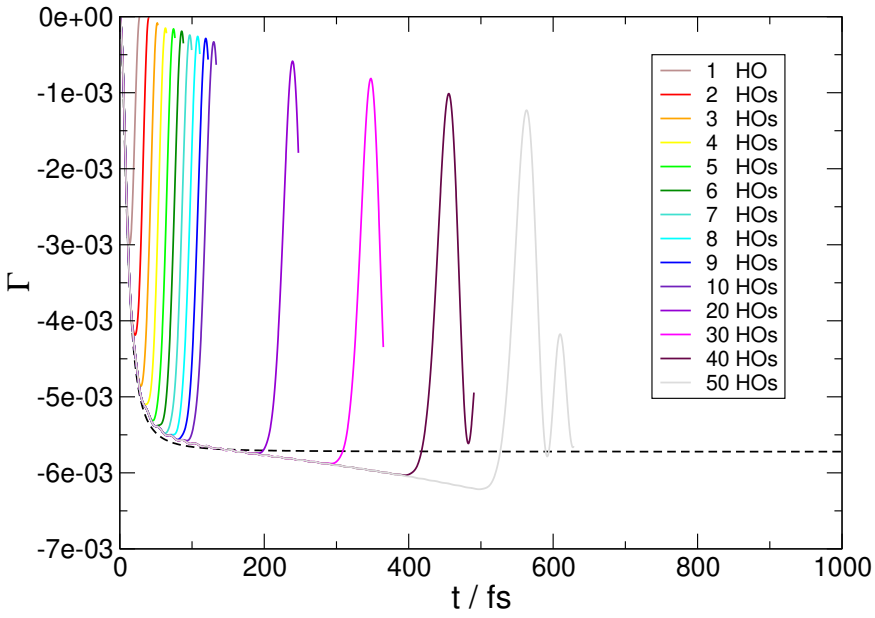

Figure 7.3: Memory kernel for different bath dimensions.

7.2 Convergence test

In order to check if a dimensional reduction was possible, we computed the transmission coefficient at $T = 100$ K and $\gamma = 0.95\ \omega_b$ for different baths, considering a number of HOs between 10 and 60. For each bath, we firstly chose the number of grid points and built the tree structure of the multilayer.

7.2.1 Simulation parameters

The ML trees chosen are shown in Fig. 7.4 and Fig. 7.5, where the number of grid points for each mode is written on the branches of the last layer. Since the high excitation is a low frequency mode characteristic, in this representation we do not need to employ of a large number of grid points. Moreover, for the same reason the Monte Carlo sampling provides fewer initial wave-packets, with a sampling weight > 1. These two consequences of the new frequency discretization incredibly reduce the computational effort, and make the effective mode representation a really powerful approach.

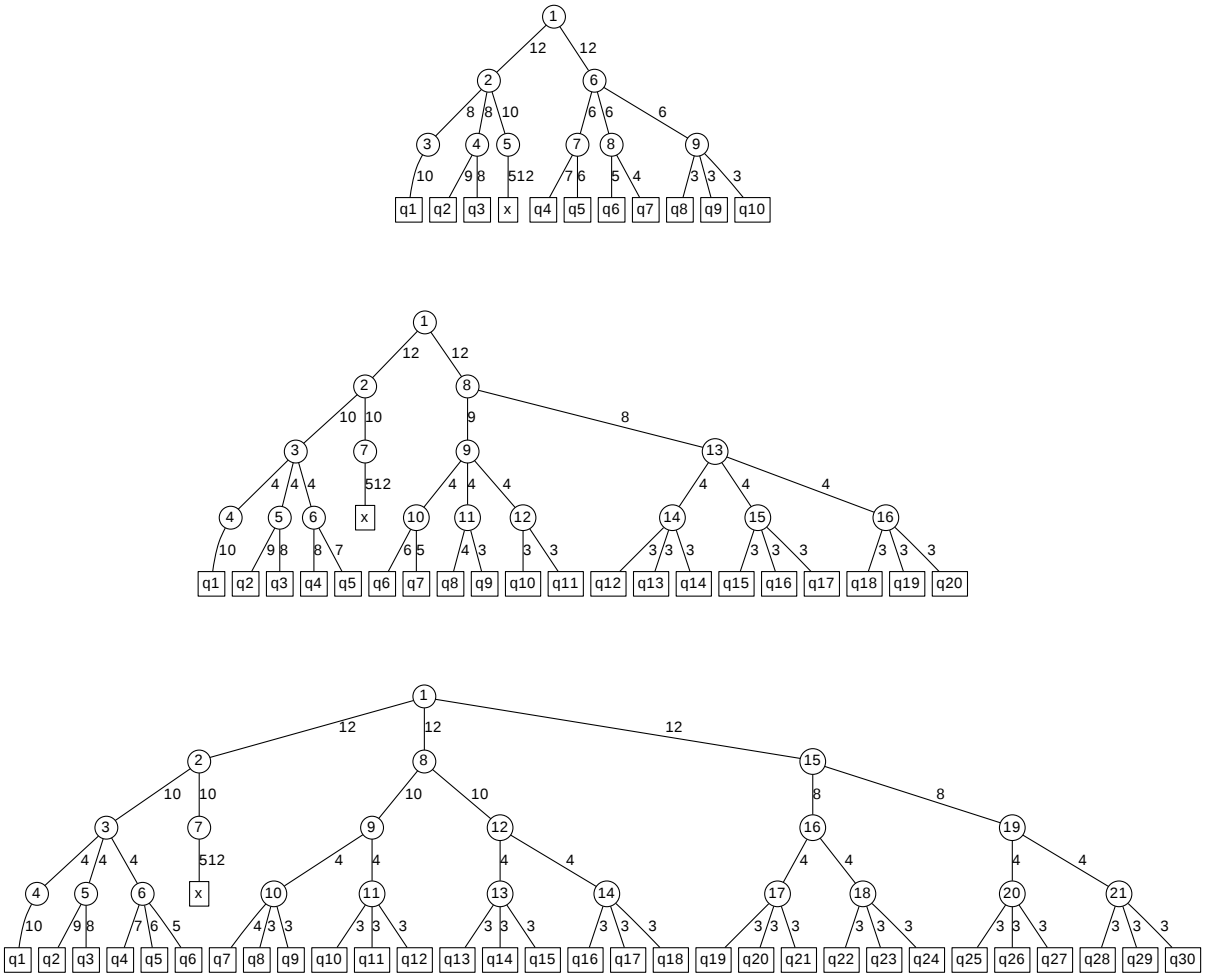

Figure 7.4: ML trees chosen for baths composed by 10, 20 and 30 effective modes.

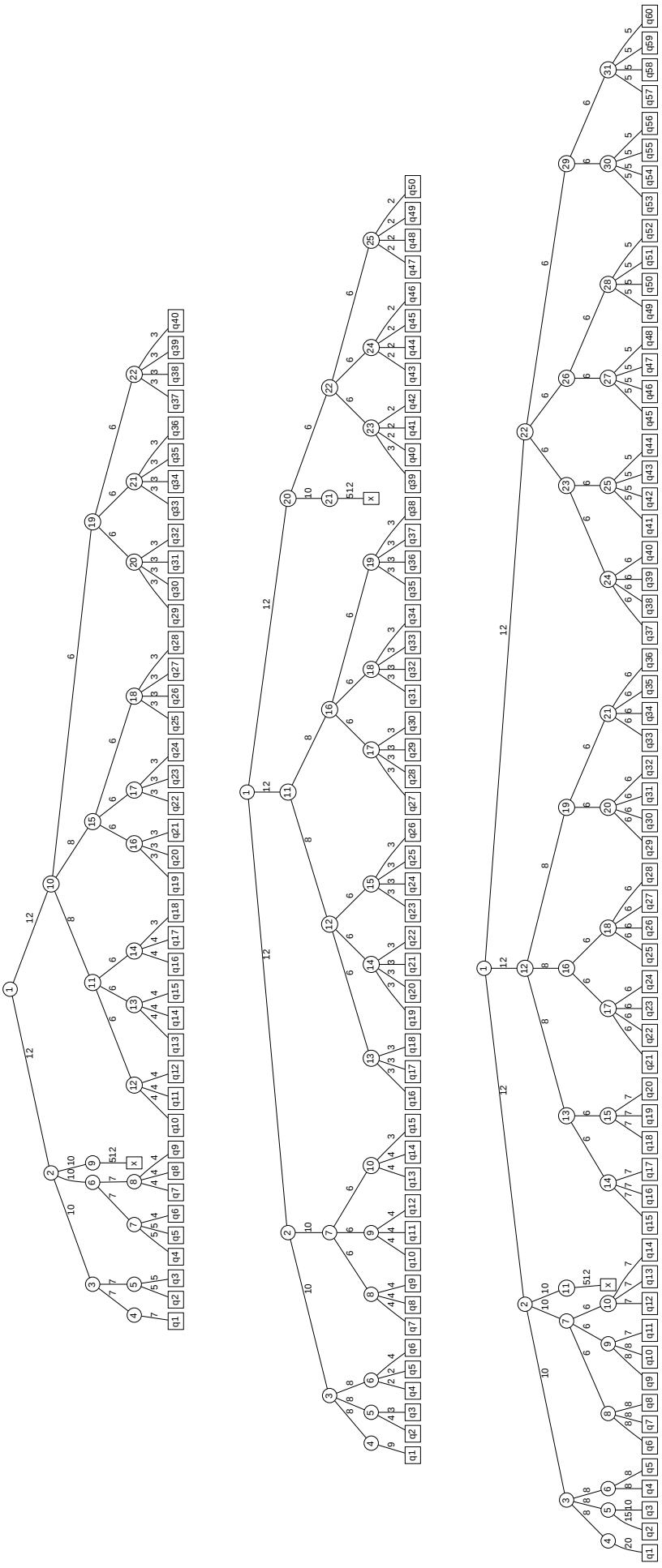

Figure 7.5: ML trees chosen for baths composed by 40, 50 and 60 effective modes.

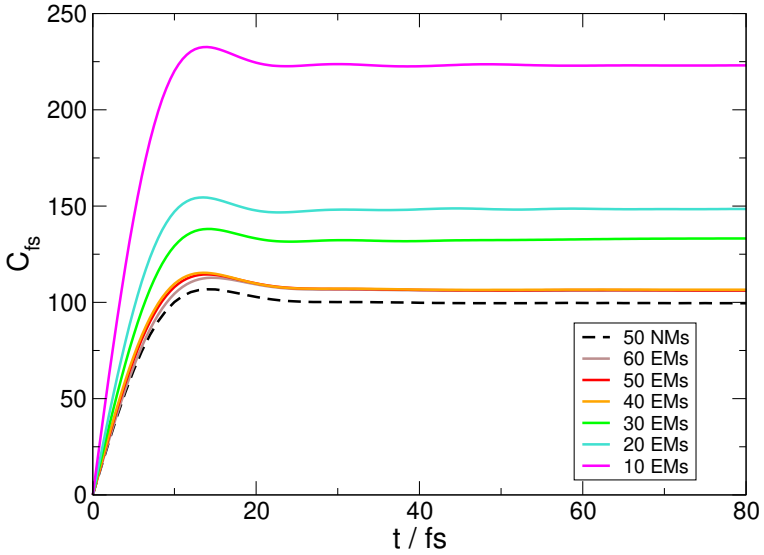

Figure 7.6: Time dependent transmission coefficient, obtained for different number of bath modes.

7.2.2 Results

From Fig. 7.3 we can estimate that for more than 10 HOs characterized by the effective modes parameters (here express as EMs) the memory effects do not occur for a time $t \tilde{<} 90$ fs. Thus, we performed dynamics up to $t = 80$ fs, and the results for time dependent transmission coefficients are shown in Fig. 7.6. The curves obtained for baths of different dimensions have the same shape, while the plateau value decreases as a function of the number of effective modes employed. For 40, 50 and 60 EMs the same $\kappa(\tau_P)$ is reached with a perfect overlap, proving this partition to be effective in reducing the wave-packet dimension without losing accuracy. The black dashed line is the result obtained with the previous bath parameters, i.e. the normal mode discretization, with 50 bath degrees of freedom (here express as NMs). The two representations are in excellent agreement, providing slightly different results ($\Delta k/k_{NM} \simeq 6\%$).

Chapter 8

Asymmetric potential

The DW system studied in the previous chapters is characterized by an optimal overlap between the metastable states of each well. As a result, the dynamics can be described by coherent tunneling between such states. This term opposes to the often considered process where the metastable state is left to decay out of the metastable well (by tunneling) and never comes back to its original position. In order to investigate the role that resonance plays for determining the rate, we built an asymmetric double well potential.

8.1 Model potential

It is possible to build an asymmetric potential modifying the DW model, starting from equation in Eq 4.1

$$V_0(s) = \frac{m^2\omega_m^4}{64E_b}s^4 - \frac{m\omega_m^2}{4}s^2$$

We devise a transition function that allows us to tune its product well depth, controlled by the depth factor a:

$$f(x;a) = 1 + \frac{a}{e^{1+\frac{1}{x^2}}} \tag{8.1}$$

guaranteeing that both well minimum position, the reagent well depth, its width and the frequency at the top of the barrier remain fixed. The latter is a fundamental condition for the Transition State Theory rate and its semi-classical corrections to be unaffected by changes in the potential. The final system potential energy function is piecewise defined, and reads as

$$V(x;a) = \begin{cases} V_0(x) & x \leq 0 \\ \\ V_0(x) \cdot f(x;a) & x > 0 \end{cases} \tag{8.2}$$

a is an arbitrary number which allows us to linearly increase the product well depth. Fig. 8.1 shows asymmetric potentials built for different values of a. The dashed lines mark the energy values of the product minimum E_w, computed as

$$E_w^{(a)} = E_w^{(0)} + \left(E_w^{(1)} - E_w^{(0)}\right) a \tag{8.3}$$

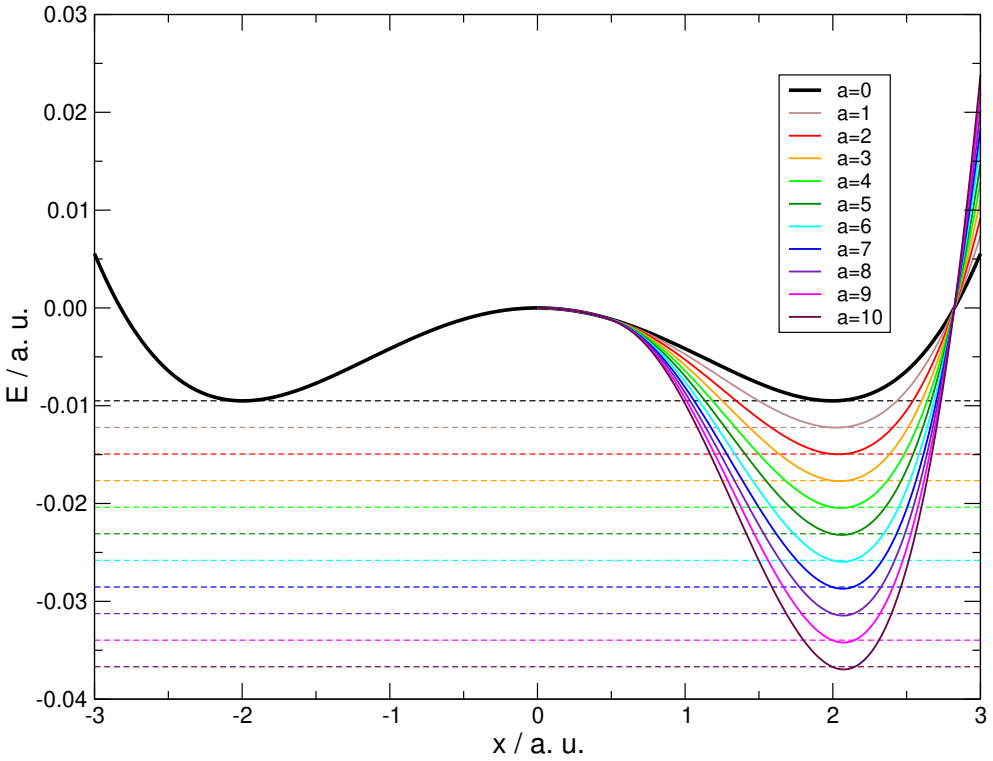

Figure 8.1: Different potentials as a function of parameter a.

The perfect overlap of values calculated with Eq. 8.3 and derived from Eq. 8.2 proves the linear proportion between the product well depth and the parameter a, giving a complete control on potential modifications.

8.1.1 Overlap study

In order to make a prediction on the resonance role in the dynamics, we computed the system Hamiltonian eigenvalues as a function of the product depth factor. Their overlap are shown in Fig. 8.2 and resonant states appear for $a = 1.56$, 3.71 and 6.52. Fig. 8.3 shows the potential energy curves obtained with four values of a, characterized by their proper eigenstates. Starting from the coherent case ($a = 0$), the Ground State (GS) of the two wells are in resonance (top left panel). Increasing the depth factor ($a = 0.5$) the two GSs are characterized by different energy, and the resonance is broken (top right panel). The reagent GS is in the middle between two states of the product well, and its first excited state (Ex1) approaches the energy of reagent GS as a increases ($a = 1$, bottom left panel). When Ex1 has exactly the same energy of the reagent GS ($a = 1.56$) we are in the resonance regime, and the eigenstate overlap leads to the formation of the tunneling splitting described in Section 4.1.1.

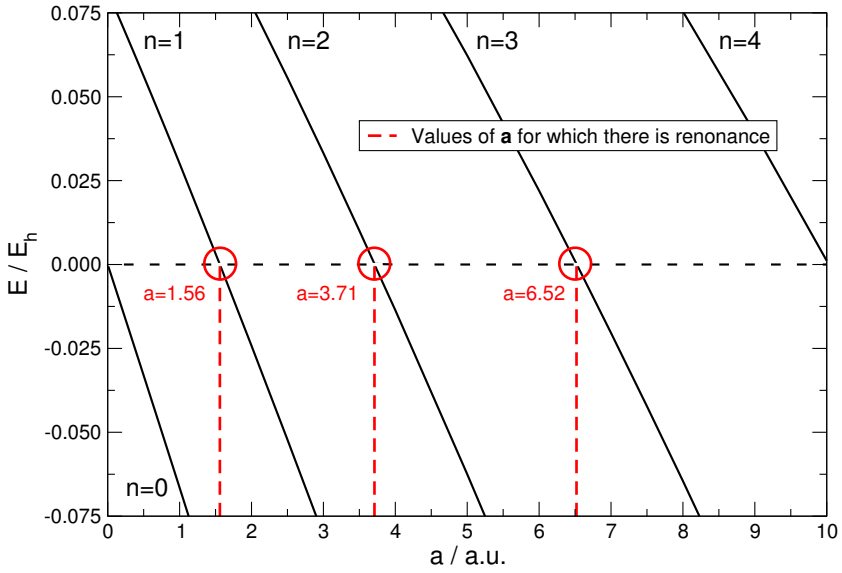

Figure 8.2: Product eigenstate energy as a function of a.

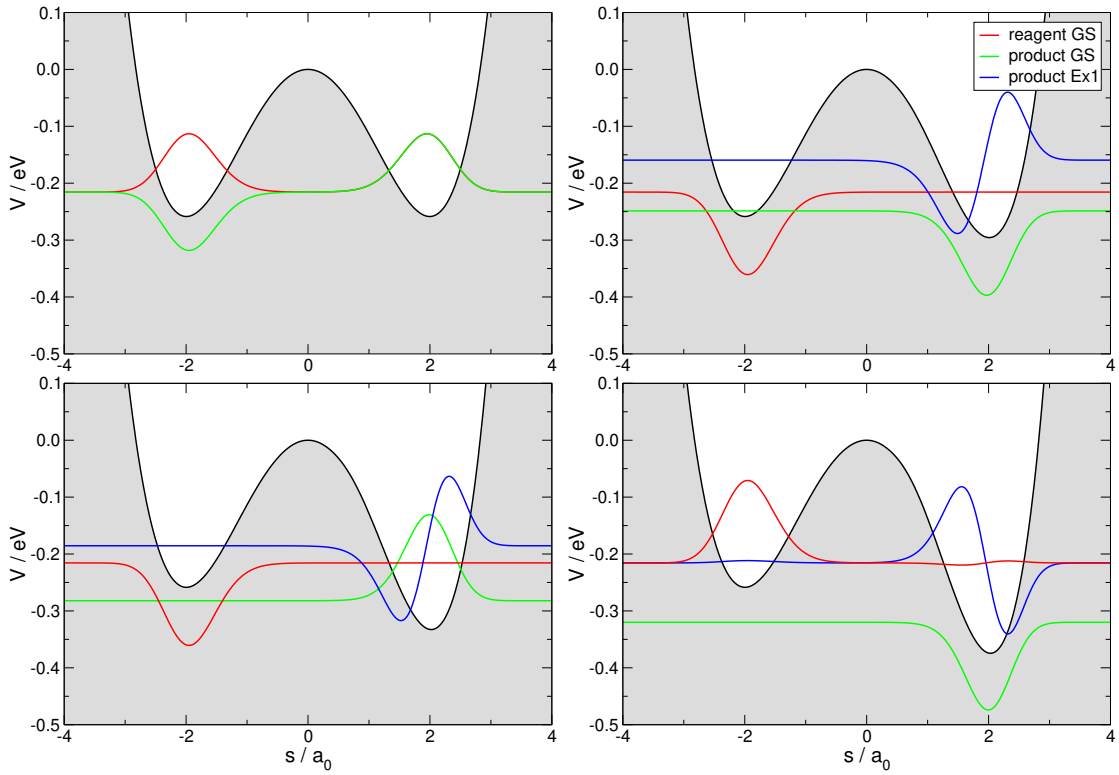

Figure 8.3: Eigenstates for different asymmetric potentials. Top-left: a=0; top-right: $a = 0.5$; bottom-left: $a = 1$; bottom-right: $a = 1.56$.

8.2 Results

For this problem we considered a quite strong friction regime, $\gamma = 0.95\omega_b$, and we studied transmission coefficients as a function of a for $T = 300$ K and $T = 100$ K.

At high temperature it is not possible to distinguish a trend, as shown in Fig. 8.4. $\kappa(a)$ oscillates randomly within $\pm 1.3\%$ of $\kappa(0)$, i.e. around the transmission coefficient obtained for the symmetric potential (black dotted line). Moreover, no significant variations are present in correspondence of a resonant state (red dashed lines), i.e. $\kappa(a)$ is not affected by resonance. In classical regime, in fact, quantum effects do not play an important role in the dynamics, so coherent tunneling is negligible.

At low temperature we observe an oscillating trend: κ increases up to a maximum for $a \simeq 0.8$, decreases to a minimum in correspondence of $a \simeq 1.2$, and increases faster changing its convexity for $a = 1.56$. This behavior is due to two different effects. The initial linear increase for really small values of a is a collateral effect due to how we built the potential: in order to maintain the minimum position fixed, we unavoidably contract the energy barrier, thus tunneling is easier and κ increases.

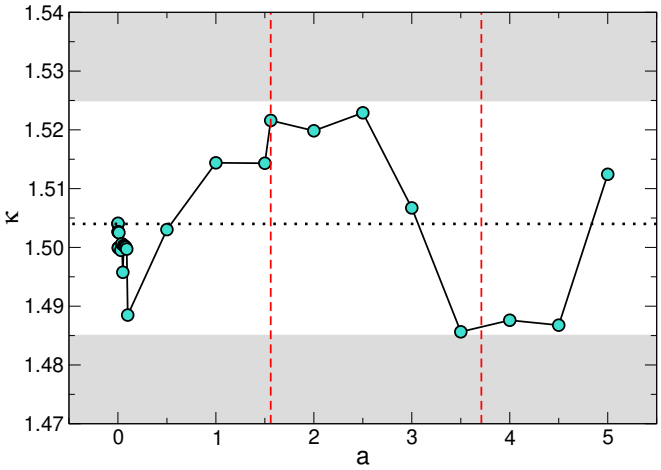

Figure 8.4: Transmission coefficient as a function of a at $T = 300$ K.

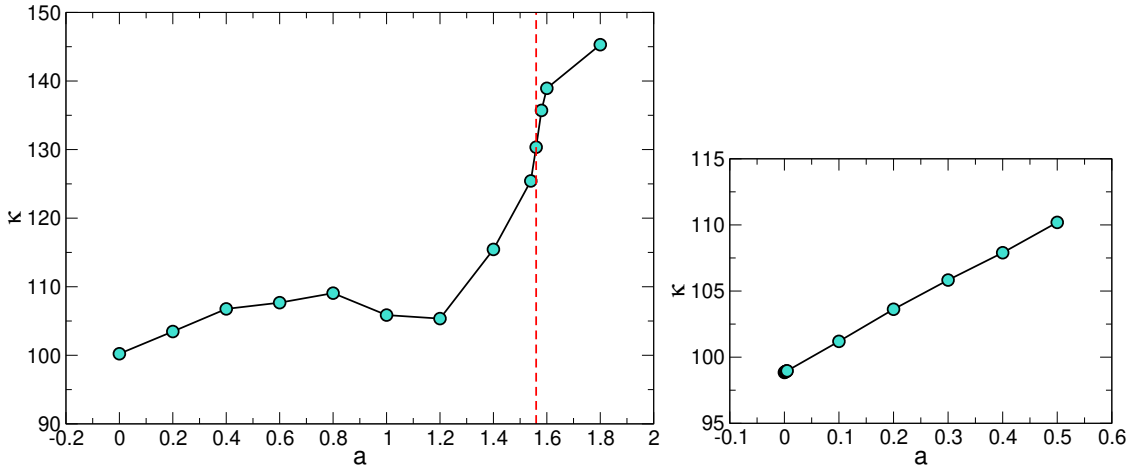

Figure 8.5: Transmission coefficient as a function of a at $T = 100$ K; on the right a zoom in on the region of small depth increase.

Turning away from the resonant state ($a = 0$), the resonance breakdown becomes more important than the barrier contraction, leading to the κ decrease. Approaching the second resonant state ($a = 1.56$) the two effects are added together, leading to a fast increase. This sort of oscillating trend is expected even for a wider range of a, in correspondence of each resonant state, but we faced a lot of convergence problems for the correlation function that we approached as explained in the following section.

8.2.1 Energy filter

We performed several tests, in which we increased grid points and SPFs for the bath modes, and the correlation functions obtained are plotted in Fig. 8.6. Increasing the number of grid points does not significantly affect the results, while the number of SPFs provides a little improvement.

Since we have not been able to overcome the problem considering the real time propagation, we focused on the relaxation, in particular on the dissipated energy of each sampling. Fig. 8.7 shows the integral of the energy dissipated during the imaginary propagation as a function of the energy of the sampling. The different curves represent each depth considered for the product well ($a = 0.1 - 2.0$), in ascending order starting from the bottom. The depth factor that characterizes two adjacent curves is monospaced, so we did not expect a so large distance from the blue curve ($a = 1.8$) and the yellow one ($a = 1.9$). On the basis of this plot we applied three different filters, at a sampling energy of 14.5, 8.5 and 6, in order to eliminate those wave-packets characterized by an energy in the fluctuating part of the graph. Since the results improved with the SPF increase (Fig. 8.6), we considered three different kind of ML trees, keeping fixed the branch structure but setting more SPFs for each of them. More in detail

$$\text{SPFs(ML-sdt)} < \text{SPFs(ML-aug)} < \text{SPFs(ML-plus)}$$

For each ML the results improve after the filtering (Figs. 8.8, 8.9 and 8.10), but not as we can expect. For a worse filter the result quality is in the order:

$$\text{ML-aug} > \text{ML-sdt} > \text{ML-plus}$$

while for a better one we have:

$$\text{ML-plus} > \text{ML-sdt} > \text{ML-aug}$$

probably because of the sum of several computational approximations. As the filter becomes more restrictive the number of samplings taken into account reduces, passing from 204 to 54, wasting $\sim 75\%$ of the dynamics. For this reason it would be necessary to sample more initial wave-packets, but at least 1000 imaginary time propagations would need to be run, filtered and only the $\sim 25\%$ of the wave-packets would be evolved in real time. Moreover, the SPFs increase leads to a result improvement only for a very restricted filter, and we should also consider the expensive computation cost due to the SPF number.

The problem of asymmetric potentials, proved to be a tough numerical task that we were unable to solve in the presence of marked asymmetries, despite many efforts and the use of alternative approaches and tricks (in a collaborative effort with Professor Fermín Huarte Larrañaga at Universitat de Barcelona).

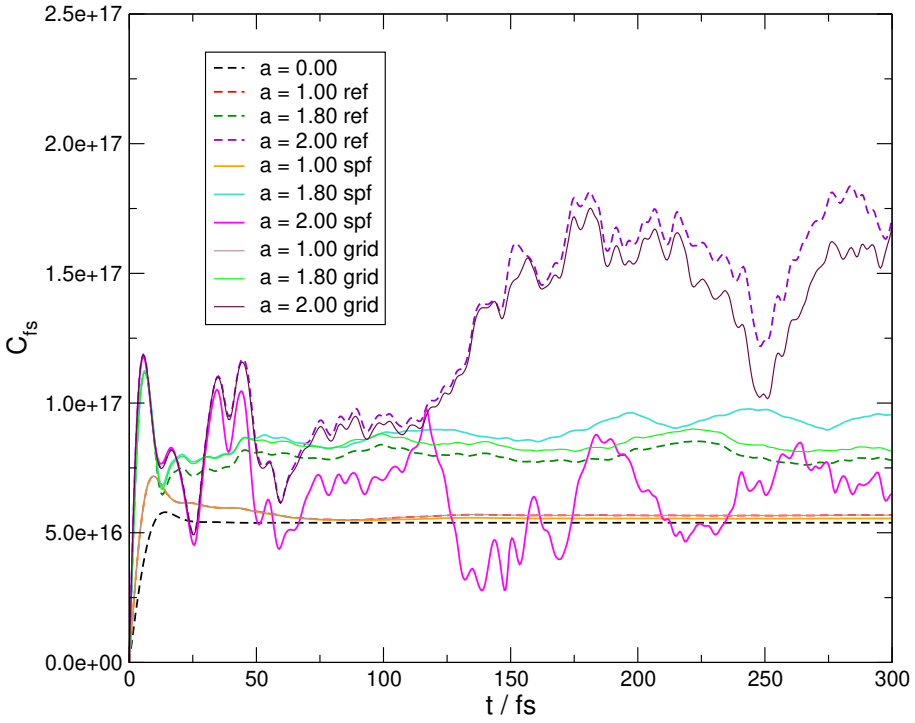

Figure 8.6: Correlation function as a function of time for different depth of the product well. Results obtained with the structure used till now (ref), with the augmented grid (grid), and increasing the number of SPFs for each tree branch (spf).

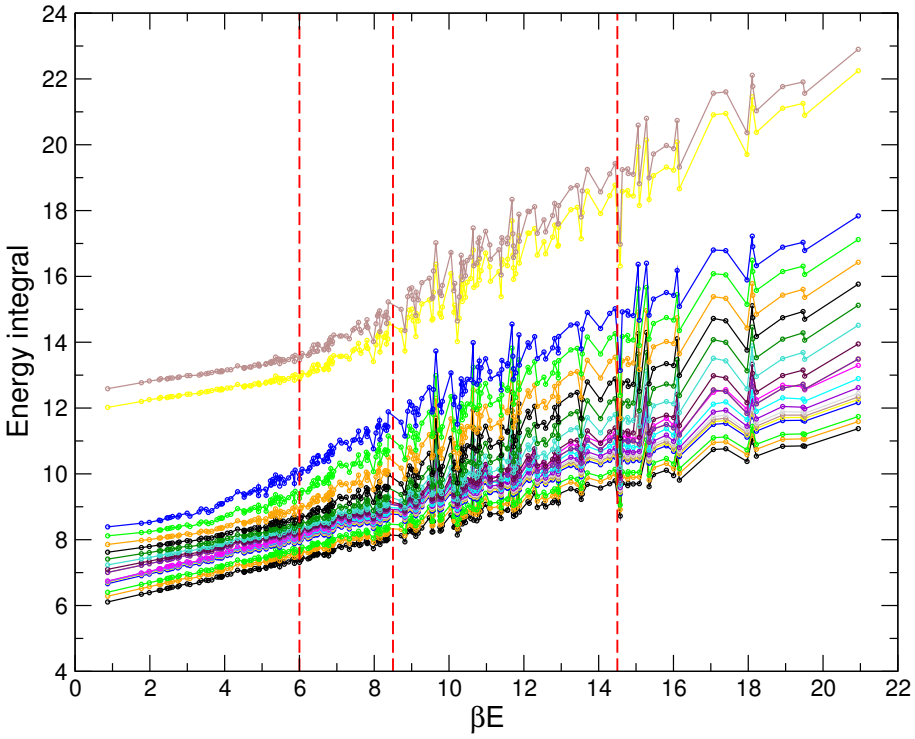

Figure 8.7: Energy dissipated integral as a function of sampling energy.

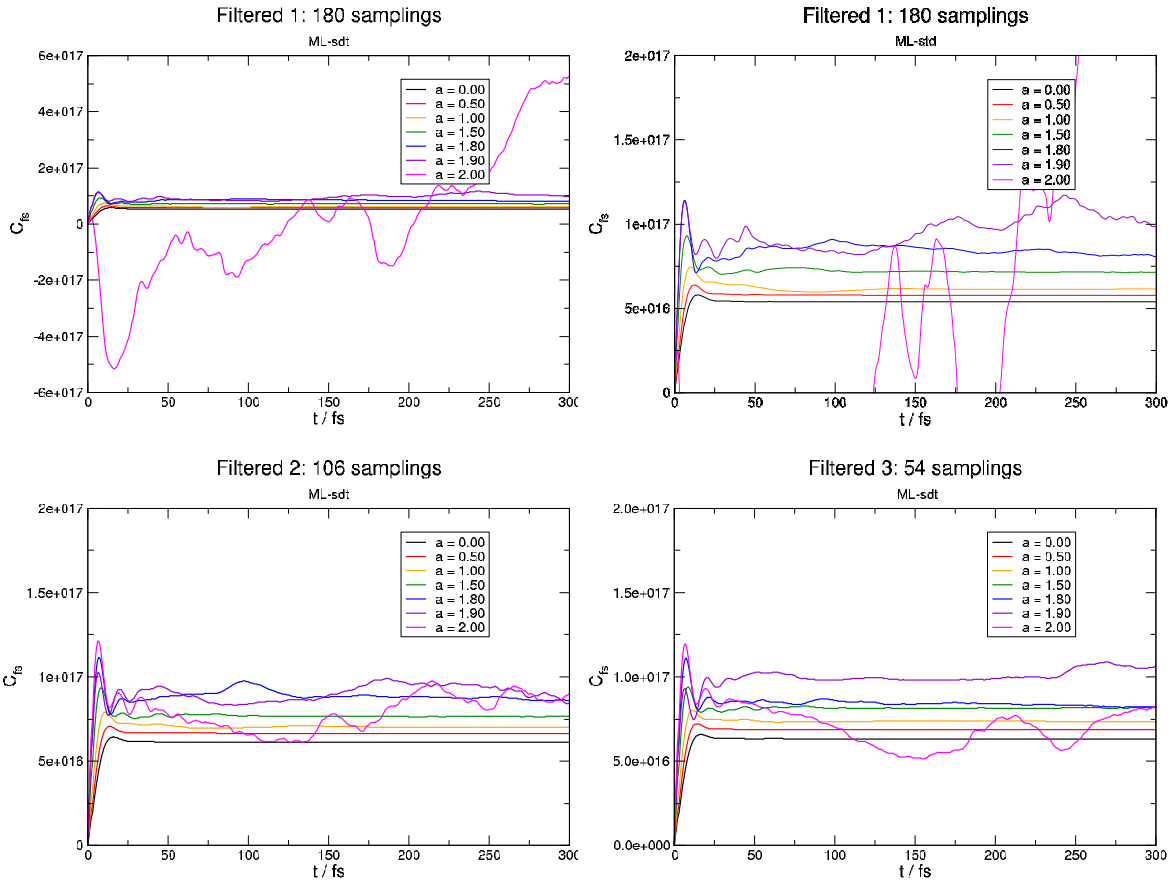

Figure 8.8: ML-sdt after different filtering: correlation functions as a function of time for each depth of the well considered.

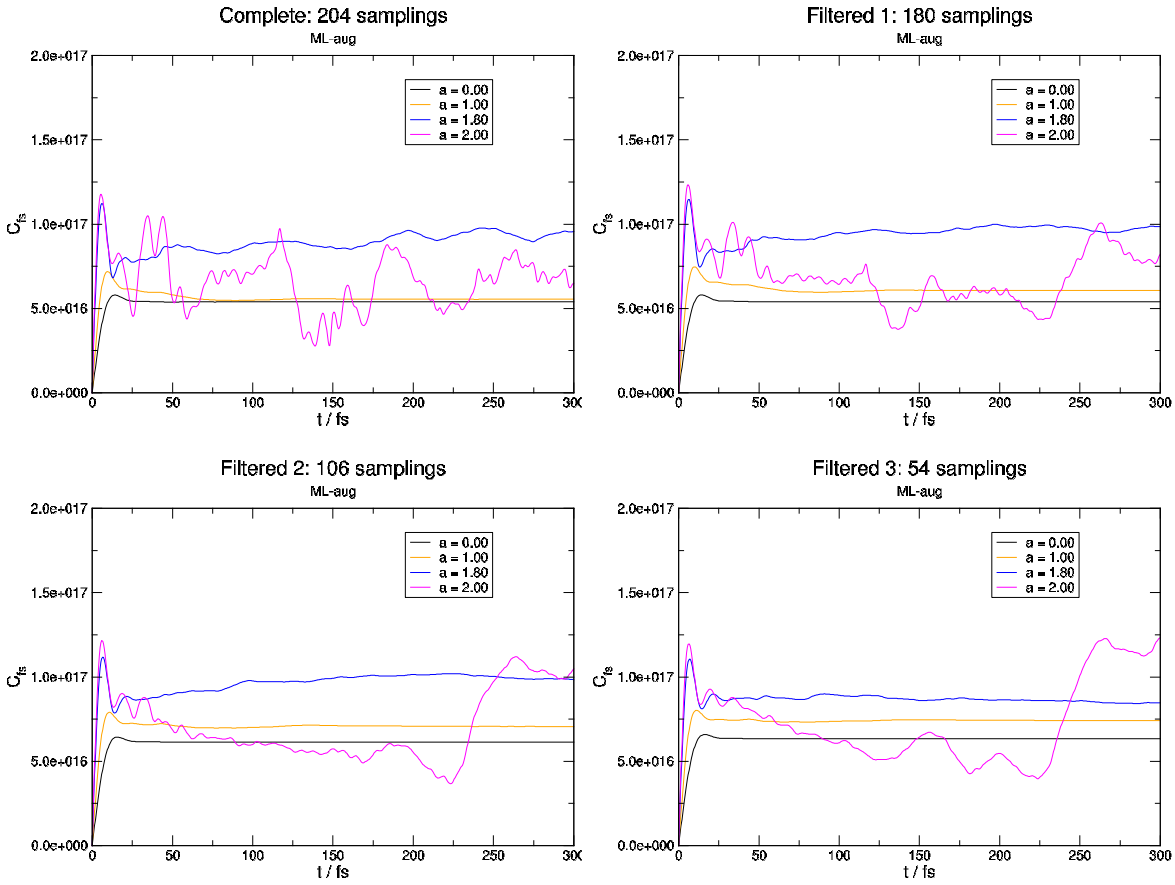

Figure 8.9: ML-aug after different filtering: correlation functions as a function of time for each depth of the well considered.

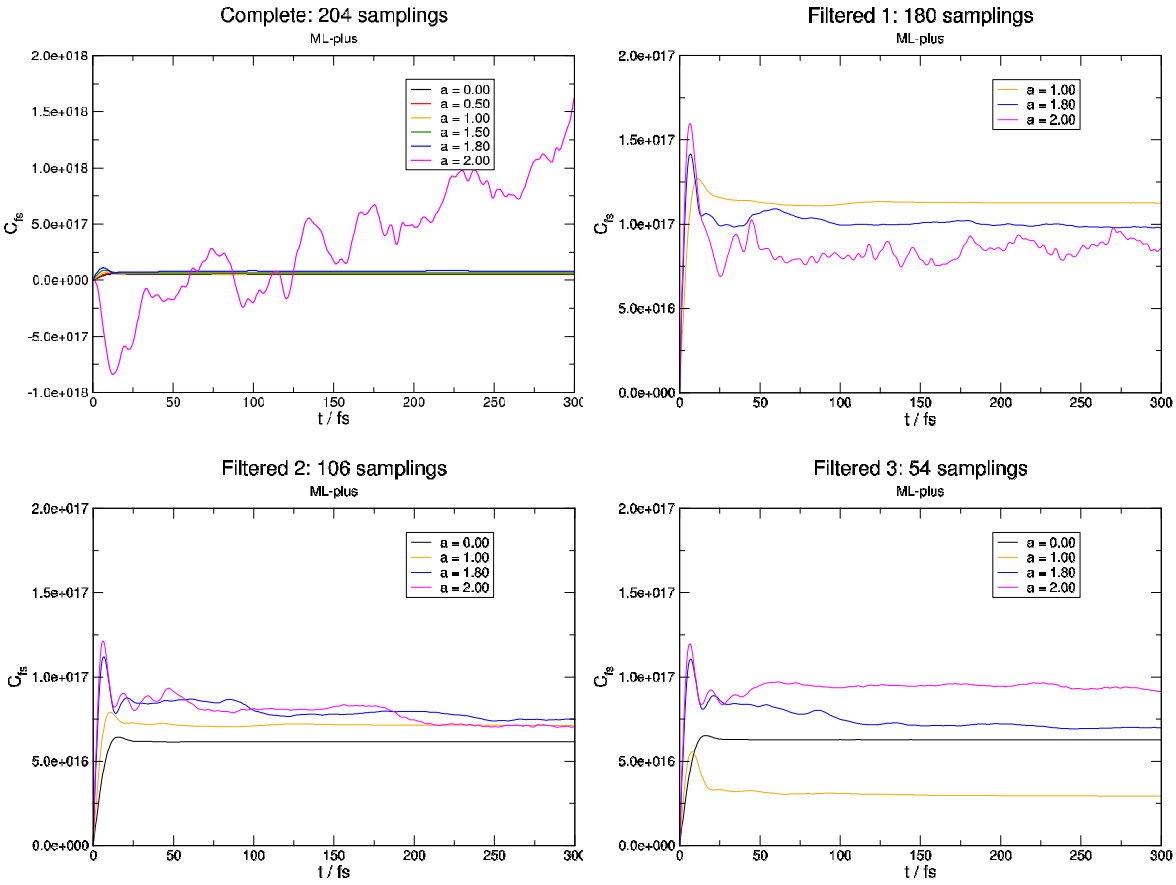

Figure 8.10: ML-plus after different filtering: correlation functions as a function of time for each depth of the well considered.

Chapter 9

Conclusions

From the study conducted for this thesis we obtained results for a wide range of temperature and friction regimes, that provided a complete picture of what happens in different reaction conditions for condensed phase processes.

The work on the symmetric DW potential, already studied in the literature, proved our procedure's reliability. We could distinguish the classical regime, in which the transmission coefficient is characterized by the Kramers' turnover, and the quantum one, where the kinetic constants tends to a plateau determined by tunneling. Moreover, we found the quantum-classical crossover point for intermediate temperatures and extremely low frictions. The transmission coefficient as a function of friction is characterized by a mixture between classical and quantum behaviour: in these delicate conditions, thermal fluctuation and tunneling are equally important, and the dynamics is ruled by a balance between them.

The results at low temperatures turned out to be extremely useful as benchmarks for RPI calculations, but further studies are needed in order to expand the data comparable with that method.

The employment of the effective mode discretization of the bath extremely reduced the computational effort needed. The new frequency distribution within the bath modes, and the consequent occupation of lower states, allowed us to employ fewer grid points and reduced the number of the initial wave packets sampled with the Monte Carlo approach. Additionally, our calculations proved that 40 HOs yield the same result as more HOs, i.e. with this new representation it is possible to employ fewer bath modes than with the normal mode discretization without loss of accuracy.

The asymmetric problem, applicable as 1D model for the physisorption - chemisorption transition, remains a challenge (apparently not yet settled in the literature), but our study could provide a hint at what to expect from further investigations.

Bibliography

[1] ESO, VLT, HAWK-I, H. Drass et al.
(https://cdn.eso.org/images/thumb700x/eso1625a.jpg)

[2] Garczarek, Florian, and Klaus Gerwert. "Functional waters in intraprotein proton transfer monitored by FTIR difference spectroscopy." Nature 439.7072 (2006): 109.

[3] Knapp, Michael J., Keith Rickert, and Judith P. Klinman. "Temperature-dependent isotope effects in soybean lipoxygenase-1: correlating hydrogen tunneling with protein dynamics." Journal of the American Chemical Society 124.15 (2002): 3865-3874.

[4] Levine, Ariel D., Michael Iv, and Uri Peskin. "Length-independent transport rates in biomolecules by quantum mechanical unfurling." Chemical Science 7.2 (2016): 1535-1542.

[5] Bonfanti, Matteo, Simona Achilli, and Rocco Martinazzo. "Sticking of atomic hydrogen on graphene." Journal of Physics: Condensed Matter 30.28 (2018): 283002.

[6] https://www.researchgate.net/ii/hosted.content.attachment/
AS:733751965388801@1551951509106_xl

[7] https://stockhead.com.au/wp-content/uploads/2018/08/Graphene-2-1024x576.jpg

[8] Bonfanti, Matteo, et al. "Physisorption and diffusion of hydrogen atoms on graphite from correlated calculations on the H-coronene model system." The Journal of Physical Chemistry C 111.16 (2007): 5825-5829.

[9] Medina, Zuleika, and Bret Jackson. "Quantum studies of light particle trapping, sticking, and desorption on metal and graphite surfaces." The Journal of chemical physics 128.11 (2008): 114704.

[10] Creighan, Susan C., James SA Perry, and Stephen D. Price. "The rovibrational distribution of H 2 and HD formed on a graphite surface at 15–50 K." The Journal of chemical physics 124.11 (2006): 114701.

[11] Islam, Farahjabeen, Elspeth R. Latimer, and Stephen D. Price. "The formation of vibrationally excited HD from atomic recombination on cold graphite surfaces." The Journal of chemical physics 127.6 (2007): 064701.

[12] Latimer, Elspeth R., Farahjabeen Islam, and Stephen D. Price. "Studies of HD formed in excited vibrational states from atomic recombination on cold graphite surfaces." Chemical Physics Letters 455.4-6 (2008): 174-177.

[13] Hollenbach, David, and E. E. Salpeter. "Surface recombination of hydrogen molecules." The Astrophysical Journal 163 (1971): 155.

[14] Martinazzo, Rocco, Simone Casolo, and Liv H. Hornekær. "Hydrogen Recombination on Graphitic Surfaces." Dynamics of Gas-Surface Interactions. Springer Berlin Heidelberg, 2013. 157-177.

[15] https://cdn2.picryl.com/photo/2011/08/15/graphene-in-space-artist-concept-0a86b2-640.jpg

[16] https://www.spacenewsfeed.com/images/2018-june/experiments-2.jpg

[17] ALMA (ESO/NAOJ/NRAO), M. Maercker et al. (https://cdn.eso.org/images/thumb700x/eso1239a.jpg)

[18] Affleck, Ian. "Quantum-statistical metastability." Physical Review Letters 46.6 (1981): 388.

[19] Gillan, M. J. "Quantum-classical crossover of the transition rate in the damped double well." Journal of Physics C: Solid State Physics 20.24 (1987): 3621.

[20] Gol'danskii, V. I. Dokl. Akad. Nauk SSSR 124-127, 1261 (1959)

[21] Hänggi, Peter, et al. "Quantum theory of activated events in presence of long-time memory." Physical review letters 55.7 (1985): 761.

[22] Kramers, Hendrik Anthony. "Brownian motion in a field of force and the diffusion model of chemical reactions." Physica 7.4 (1940): 284-304.

[23] Hänggi, Peter, Peter Talkner, and Michal Borkovec. "Reaction-rate theory: fifty years after Kramers." Reviews of modern physics 62.2 (1990): 251.

[24] Lee, Minyung, G. R. Holtom, and Robin M. Hochstrasser. "Observation of the Kramers turnover region in the isomerism of trans-stilbene in fluid ethane." Chemical physics letters 118.4 (1985): 359-363.

[25] Leggett, Anthony J., et al. "Dynamics of the dissipative two-state system." Reviews of Modern Physics 59.1 (1987): 1.

[26] Bonfanti, Matteo, et al. "Quantum dynamics of hydrogen atoms on graphene. II. Sticking." The Journal of chemical physics 143.12 (2015): 124704.

[27] Miller, William H. "Classical-limit quantum mechanics and the theory of molecular collisions." Adv. Chem. Phys 25.1 (1974): 69-177.

[28] Miller, William H., Steven D. Schwartz, and John W. Tromp. "Quantum mechanical rate constants for bimolecular reactions." The Journal of chemical physics 79.10 (1983): 4889-4898.

[29] Yamamoto, Takeshi, Haobin Wang, and William H. Miller. "Combining semiclassical time evolution and quantum Boltzmann operator to evaluate reactive flux correlation function for thermal rate constants of complex systems." The Journal of chemical physics 116.17 (2002): 7335-7349.

[30] Bonfanti, Matteo, et al. "Quantum dynamics of hydrogen atoms on graphene. I. System-bath modeling." The Journal of chemical physics 143.12 (2015): 124703.

[31] Ford, George W., John T. Lewis, and R. F. O'connell. "Quantum langevin equation." Physical Review A 37.11 (1988): 4419.

[32] https://i1.wp.com/www.purochamuyo.com/wp-content/uploads/2016/09/disipacion.png

[33] Ford, G. W., J. T. Lewis, and R. F. O'connell. "Independent oscillator model of a heat bath: exact diagonalization of the Hamiltonian." Journal of statistical physics 53.1-2 (1988): 439-455.

[34] Caldeira, Amir O., and Anthony J. Leggett. "Path integral approach to quantum Brownian motion." Physica A: Statistical mechanics and its Applications 121.3 (1983): 587-616.

[35] Zwanzig, Robert. "Nonlinear generalized Langevin equations." Journal of Statistical Physics 9.3 (1973): 215-220.

[36] Gross, D. H. E. "Deep inelastic collisions viewed as brownian motion." Deep-inelastic and fusion reactions with heavy ions. Springer, Berlin, Heidelberg, 1980. 81-90.

[37] Cederbaum, Lorenz S., Etienne Gindensperger, and Irene Burghardt. "Short-time dynamics through conical intersections in macrosystems." Physical review letters 94.11 (2005): 113003.

[38] Gindensperger, Etienne, Irene Burghardt, and Lorenz S. Cederbaum. "Short-time dynamics through conical intersections in macrosystems. I. Theory: Effective-mode formulation." The Journal of chemical physics 124.14 (2006): 144103.

[39] Gindensperger, Etienne, Irene Burghardt, and Lorenz S. Cederbaum. "Short-time dynamics through conical intersections in macrosystems. II. Applications." The Journal of chemical physics 124.14 (2006): 144104.

[40] Hughes, Keith H., Clara D. Christ, and Irene Burghardt. "Effective-mode representation of non-Markovian dynamics: A hierarchical approximation of the spectral density. I. Application to single surface dynamics." The Journal of chemical physics 131.2 (2009): 024109.

[41] Martinazzo, R., K. H. Hughes, and I. Burghardt. "Unraveling a Brownian particle's memory with effective mode chains." Physical Review E 84.3 (2011): 030102.

[42] Burghardt, Irene, Rocco Martinazzo, and Keith H. Hughes. "Non-Markovian reduced dynamics based upon a hierarchical effective-mode representation." The Journal of chemical physics 137.14 (2012): 144107.

[43] Wang, Haobin, David E. Skinner, and Michael Thoss. "Calculation of reactive flux correlation functions for systems in a condensed phase environment: A multilayer multiconfiguration time-dependent Hartree approach." The Journal of chemical physics 125.17 (2006): 174502.

[44] Craig, Ian R., Michael Thoss, and Haobin Wang. "Proton transfer reactions in model condensed-phase environments: Accurate quantum dynamics using the multilayer multiconfiguration time-dependent Hartree approach." The Journal of chemical physics 127.14 (2007): 144503.

[45] Meyer, H. D., Uwe Manthe, and Lorenz S. Cederbaum. "The multi-configurational time-dependent Hartree approach." Chemical Physics Letters 165.1 (1990): 73-78.

[46] Beck, Michael H., et al. "The multiconfiguration time-dependent Hartree (MCTDH) method: a highly efficient algorithm for propagating wavepackets." Physics reports 324.1 (2000): 1-105.

[47] http://www.pci.uni-heidelberg.de/cms/mctdh.html

[48] Wang, Haobin. "Multilayer multiconfiguration time-dependent Hartree theory." The Journal of Physical Chemistry A 119.29 (2015): 7951-7965.

[49] Meyer, Hans-Dieter. "Studying molecular quantum dynamics with the multiconfiguration time-dependent Hartree method." Wiley Interdisciplinary Reviews: Computational Molecular Science 2.2 (2012): 351-374.

[50] Topaler, Maria, and Nancy Makri. "Quantum rates for a double well coupled to a dissipative bath: Accurate path integral results and comparison with approximate theories." The Journal of chemical physics 101.9 (1994): 7500-7519.

[51] Weiss, U. "Quantum Dissipative Systems, vol. XIII." (1993).

[52] Grote, Richard F., and James T. Hynes. "The stable states picture of chemical reactions. II. Rate constants for condensed and gas phase reaction models." The Journal of Chemical Physics 73.6 (1980): 2715-2732.

[53] Wolynes, Peter G. "Quantum theory of activated events in condensed phases." Physical Review Letters 47.13 (1981): 968.

[54] Pollak, Eli. "Transition state theory for quantum decay rates in dissipative systems: the high-temperature limit." Chemical physics letters 127.2 (1986): 178-182.

[55] Christov, St G. "The characteristic (crossover) temperature in the theory of thermally activated tunneling processes." Molecular Engineering 7.1-2 (1997): 109-147.

[56] Christov, St G. "Verallgemeinerte Näherungsausdrücke für die Durchlässigkeit von Potentialschwellen." Annalen der Physik 467.1-2 (1963): 20-31.

[57] Christov, St G. "Electron transitions through and over potential barriers in solids." physica status solidi (b) 42.2 (1970): 583-589.

[58] Christov, St G. "Die Rolle des Tunnelübergangs der Ionen in der Kinetik der Elektrodenvorgänge." Zeitschrift für Elektrochemie, Berichte der Bunsengesellschaft für physikalische Chemie 62.5 (1958): 567-581.

[59] Christov, St G., Dokl. Akad. Nauk SSSR 136, 663 (1960).

[60] Segal, Dvira, et al. "Electron transfer rates in bridged molecular systems 2. A steady-state analysis of coherent tunneling and thermal transitions." The Journal of Physical Chemistry B 104.16 (2000): 3817-3829.

[61] Grabert, Hermann, Ulrich Weiss, and Peter Hänggi. "Quantum tunneling in dissipative systems at finite temperatures." Physical review letters 52.25 (1984): 2193.

[62] Richardson, Jeremy O. "Ring-polymer instanton theory." International reviews in physical chemistry 37.2 (2018): 171-216.

[63] Richardson, Jeremy O. "Ring-polymer instanton theory of electron transfer in the nonadiabatic limit." The Journal of chemical physics 143.13 (2015): 134116.

[64] Richardson, Jeremy O. "Perspective: Ring-polymer instanton theory." The Journal of chemical physics 148.20 (2018): 200901.

[65] Laude, Gabriel, et al. "Ab initio instanton rate theory made efficient using Gaussian process regression." Faraday discussions 212 (2018): 237-258.